Distribution Agreement

In presenting this thesis as a partial fulfillment of the requirements for a degree from Emory University, I hereby grant to Emory University and its agents the non-exclusive license to archive, make accessible, and display my thesis in whole or in part in all forms of media, now or hereafter now, including display on the World Wide Web. I understand that I may select some access restrictions as part of the online submission of this thesis. I retain all ownership rights to the copyright of the thesis. I also retain the right to use in future works (such as articles or books) all or part of this thesis.

Sohee Chun April 6, 2021

General relativistic magnetohydrodynamic (GRMHD) simulations of black hole accretion and jets

By

Sohee Chun

Dr. Erin Bonning
Advisor

Department of Physics

Dr. Erin Bonning

Advisor

Dr. Alissa Bans

Committee Member

Dr. Davide Fossati

Committee Member

2021

General relativistic magnetohydrodynamic (GRMHD) simulations of black hole accretion and jets

By

Sohee Chun

Dr. Erin Bonning

Adviser

An abstract of
a thesis submitted to the Faculty of Emory College of Arts and Sciences
of Emory University in partial fulfillment
of the requirements of the degree of
Bachelor of Science with Honors

Department of Physics

2021

Abstract

General relativistic magnetohydrodynamic (GRMHD) simulations of black hole accretion and jets

By Sohee Chun

Active galaxies with extremely high luminosity at the center have more energy than normal galaxies do. This central compact region, or active galactic nuclei (AGN), has a supermassive black hole that powers the AGN to emit such great energy. Some AGN form astrophysical jets that scale from AU to Mpc with energies ranging from few meters to tera-electronvolts. The formation of jets depends on the spin of a supermassive black hole as well as the accretion disk, but the exact mechanism remains unclear. In this project, we investigated how the spin affects the energy output of a rotating black hole using general relativistic magnetohydrodynamic (GRMHD) simulation, HARMPI. We simulated the spherically symmetric accretion (Bondi model) and determined the sonic radius of infalling matter onto a rotating black hole. We also simulated the torus around a black hole with jets and studied the relationship between the spin of a black hole, accretion rate, and energy output. Results from the simulation indicate a positive correlation between the black hole spin and the energy output and between the accretion rate and the energy output. However, no clear relation has been identified between the black hole spin and the accretion rate. We further suggest extensive studies on the accretion rate and the energy output as well as varying magnetic field strengths.

General relativistic magnetohydrodynamic (GRMHD) simulations of black hole accretion and jets

By

Sohee Chun

Dr. Erin Bonning

Adviser

A thesis submitted to the Faculty of Emory College of Arts and Sciences
of Emory University in partial fulfillment
of the requirements of the degree of
Bachelor of Science with Honors

Department of Physics

2021

Acknowledgments

I would like to acknowledge my advisor, Dr. Erin Bonning, for her continuous warm support throughout my undergraduate study. The opportunity to study with her has allowed me to grow from a girl aspiring to be like her to a young scientist with a passion for astronomy, particularly in black holes and jets. It is my first time to have such a specific and strong interest, thank you.

I would like to extend my deep gratitude to Dr. Alissa Bans for her awesome astrophysics lectures and an opportunity to do a research in young stellar objects over the summer break after my second year. The research experience brought me the joy of computing in Python and became a motivation to pursue a career in computational astrophysics.

I appreciate and respect my family who have always supported me. Without their effort, I would not have been granted this opportunity. Finally, I would like to thank my honors committee members for their sincere interests in my work, feedback, and accommodation. I appreciate your advice and guidance in strengthening my thesis.

Contents

List of Figures

List of Tables

1. Introduction and background

When a massive star with a mass between 8 to 10 solar masses reaches its later stage of evolution, it no longer has sufficient internal pressure to remain in equilibrium and therefore undergoes a gravitational collapse. The star will become a neutron star if the mass of the collapsed remnant is about $1-2$ times the mass of the sun. A collapsed remnant greater than $3-4$ solar masses is believed to become a black hole [4]. A black hole is classified into a stellar black hole with a mass up to 100 times the solar mass and a supermassive black hole with a mass of millions to billions solar masses. A stellar black hole with mass $\sim 3-100$ solar masses is formed from stellar collapse, and a supermassive black hole begins as a seed in the early universe and grows through accretion to 10^6-10^9 solar masses.

A black hole can be further categorized by its properties: rotation and charge. A static, non-rotating black hole with no electric charge is called a Schwarzschild black hole. A rotating black hole with no electric charge is called a Kerr black hole. As the universe is electrically neutral with an approximately identical number of protons and electrons, astrophysically realistic black holes do not have an electric charge. Kerr black hole is assumed to be the most common form in nature as it is formed from a spinning star or interaction with the objects with a non-zero angular momentum such as mergers.

Supermassive black holes and the galaxies co-evolve, and the supermassive black holes are

found in the nuclei of their host galaxy [5]. A supermassive black hole grows through a process of accretion, which refers to the inflow process of the matter towards the center of the mass of a system or a gravitating object. It is one of the most common processes and is the basis for the formation of different structures in the universe [6]. While most of the supermassive black holes do not accrete (quiescent or inactive black holes), some of them do accrete. The most common model of accretion is the Shakura-Sunyaev model that assumes to have Newtonian mechanics, viscous fluid, simple radiative transfer, and axisymmetry disk geometry. Another model of accretion is the Bondi model (or Bondi-Hoyle-Lyttleton accretion model) that assumes Newtonian mechanics but adiabatic fluid and spherically symmetric accretion. Bondi accretion happens in a radial direction towards the center without viscosity, which is an unrealistic scenario but allows various properties to be estimated in a simple, spherically symmetric system. This model is also a useful resource for the numerical simulation in a case where the region far from the center has insufficient resolution to be thoroughly investigated [7]. Further explanation and analysis of Bondi accretion are presented in Section 3.1.

In actively accreting systems, both stellar and supermassive black holes may accrete matter from the disk and produce an astrophysical jet spanning from few astronomical units to mega-parsecs in length [8]. Jets are streamed from the stellar, galactic, and extragalactic objects to the surrounding medium with a wide range of luminosity and a degree of collimation. The mechanisms of how jets are formed and launched have long been a subject of debate, and the theories focus on a combination of magnetic fields, the rotation of the black hole, and the accretion disk. One of the theories, the Blandford-Payne (B-P) mechanism, suggests that jets can be driven centrifugally along the poloidal magnetic field line that makes an angle of less than 60°with respect to the surface of the disk. It further explains that the toroidal component of the magnetic field powers

and collimates the jets that move perpendicular to the disk and that the flow is driven by the gas pressure in a region near the center of the disk. The angular momentum is extracted from the magnetic forces from the accretion disk, which enables matter to infall and accrete onto the compact object [9]. Another theory, known as the Blanford-Znajek (B-Z) mechanism, suggests that jets are powered from the magnetic field in the ergosphere of a rotating black hole. It demonstrates that the energy and angular momentum will be extracted electromagnetically as the magnetic field lines in a rotating black hole interact with the currents flowing in the disk and create an electrical potential difference. It further describes that the observations of both compact radio sources require the energy that is beamed along the perpendicular direction to the disk [10]. Most jet models contain some combination of B-P and B-Z mechanisms.

In fact, a black hole is commonly observed to have a strong association with relativistic jets. The recent observation of M87, an E0 galaxy at the center of the Virgo cluster, is found to have one of the closest extragalactic jets at its center [11]. Quasars, extremely luminous objects with supermassive black holes at their center, are also observed with jets, and 3C 273 and 3C 279 are examples of powerful quasars. The mechanism that describes the production of jets and how their energy from the accreted matter is associated with the power of jets remains the subject of investigation. This knowledge is important to understand the nature of the accretion process itself and the galaxy formation with the effect of the supermassive black holes [11]. Several studies suggest that there is an obvious relation between mass accretion and jet power, which may be a significant clue in resolving this question. S. W. Allen et al. made an observation of 9 elliptical galaxies and found a tight, linear relation between the Bondi accretion power and the jet power from the Chandra X-ray data [7]. The work of S. W. Allen et al. became a motivation for this project in expanding the observational result that complies with the numerical simulations.

The goal of this project is to investigate the relationship between mass accretion rate and the energy with the use of General Relativistic Magnetohydrodynamic (GRMHD) simulation. In this thesis, we summarize simulations carried out with a 3D version of High Accuracy Relativistic Magnetohydrodynamic (HARM) code HARMPI to explore the spherical accretion onto a rotating black hole (Chapter 3) and the magnetized Fishbone-Moncrief torus with jets (Chatper 4). We simulated these two scenarios and focused on (1) the density, the pressure, and the sonic radius of infalling matter onto a rotating black hole under the spherically symmetric accretion and (2) the effect of the black hole spin on the mass accretion and the energy of black holes.

We describe the structure and configuration of HARM code in detail in the following section. In Section 3, we present the results of the simulation of Bondi accretion flows, including the convergence study and the calculation of the sonic radius. In Section 4, we demonstrate how the spin parameter influences the mass accretion and the energy of black holes. Finally, we examine the application and provide possible directions for the future studies.

2. Magnetohydrodynamics (MHD)

2.1 Introduction

Magnetohydrodynamics (MHD) describes the behavior of electrically conducting fluids or flows under the presence of a magnetic field. Astrophysical objects with high electrical conductivity and magnetic fields are often explained in terms of magnetohydrodynamic characteristics [12]. Magnetic fields have significant impacts on astrophysical fluids, especially they can induce currents into a moving fluid and create forces to alter the magnetic field themselves [13]. In describing MHD, Maxwell's equations of electromagnetism are coupled with the hydrodynamic equations that describe the motion of fluids [14]. MHD plays an important role in various fields of physics, including solar physics where the sunspots or solar flares are generated by a local magnetic field in the sun, astrophysics, and space plasma physics where plasma is influenced by the galactic magnetic field, and other plasma physics in general [13]. With its wide range of applications, MHD became an important branch of physics to solve the differential equations analytically and numerically with simulations to interpret the behavior of fluids or flows.

MHD equations are a reduced set of equations of fluid dynamics and are coupled with Maxwell's equations of electromagnetism. Here, some assumptions are proposed in formulating MHD equations. It first assumes that plasma behaves like a fluid with well-defined thermodynamic quantities

such as pressure, density, and velocity, with low fluctuation. Developing a distribution function with a sufficiently large number of particles allows to establish this assumption and is widely used in fluid mechanics, thermodynamics, and statistical physics in general. The second assumption implicates that there must be a relationship between the local electric field and the current density under any plasma phenomena. The third assumption states that the plasma is electrically neutral as the astrophysical environment contains unbound positive and negative charges. When it comes to an ideal MHD, it assumes no resistivity, viscosity, thermal conduction, or radiative transfer so that the fluid can be treated as a perfect conductor [12].

2.2 General Relativistic MHD (GRMHD)

General relativistic magnetohydrodynamics (GRMHD) describes the flows along with the magnetic fields in the region of strong gravity including black holes, neutron stars, and collapsing stellar cores. One use of GRMHD is for describing the MHD turbulence driven by the magnetorotational instability (MRI) within a rotating disk and by magnetic torques within a black hole disk [15]. MRI refers to the instability of fluid that has electrical charges and is subject to the magnetic field. This fluid is affected by the magnetic force and hydrodynamical forces such as pressure and gravity. If the fluid is in differential rotation around a fixed origin, the angular velocity of rotation decreases with radial distance, causing unstable radial motion for each differential part of the fluid. This causes an accretion disk orbiting a central object to be turbulent [16]. In fact, modern accretion theory suggests that MRI is a likely mechanism of angular momentum transport and the accretion of the black hole [17]. The theory also connects the physical laws describing the motion of gas and magnetic fields near the black holes, as well as the observable phenomena of

astrophysical jets and accretion disks of the black hole systems [15].

GRMHD simulations provide the most accurate and precise physical account for the accretion flows of the black hole and assist further research on the black hole. It describes behaviors of objects such as quasars, active galactic nuclei, and core-collapse supernova, which are all powered by the central black hole's strong gravity, electromagnetic fields, and rotation. These objects are usually studied with a numerical approach because of their non-linearity, time-dependency, and intrinsic multidimensional aspects. Understanding their evolutionary processes and observational appearances demands the comprehension of a plasma with a relativistic gravitational field, a strong electromagnetic field, and a radiation field as well. The numerical approach is mostly resolved with today's algorithms and computers, but it is still limiting - GRMHD and radiative transfer codes are typically developed separately because of the limitation of combining both radiative transfer and MHD simulations. Thus, we study these objects with a non-radiating MHD model as a first step, because the plasma is treated as a fluid with fewer degrees of freedom and the negligible radiation field [18].

Another application of GRMHD is for describing how the twisted magnetic fields play an essential role in launching the outflows from rotating objects such as stars and black holes. A rotating disk with a magnetic field accelerates the outflow, which is also affected by the twisted magnetic fields and the pressure. These factors also expand the preexisting configuration of the field's azimuthal component. This process further extracts the bipolar jets that are collimated by the strong magnetic force as shown in Figure 2.1. While the twisted configuration is stabilized due to high pressure near the base of the jets, the configuration becomes unstable with increasing twist angle as the distance from the base increases [12]. GRMHD simulations are used to study jet propagation through the magnetic fields, and a number of schemes for the simulations have been developed

with consistent research.

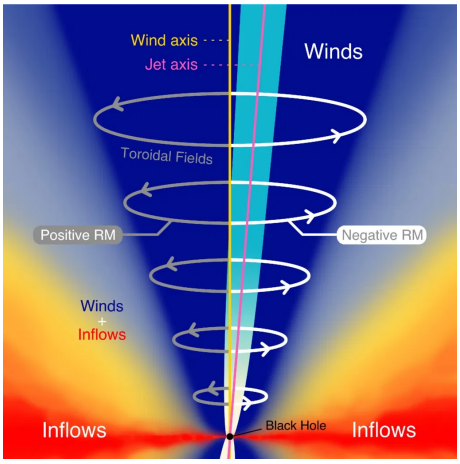

(a) Configuration of the outflows

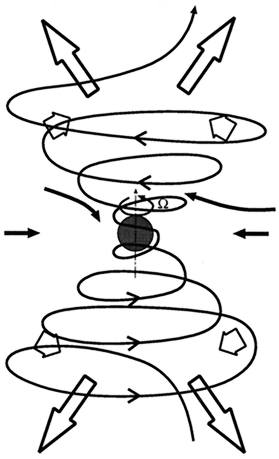

(b) Simple illustration

Figure 2.1: Both (a) and (b) show the configuration of the jets. Spinning black holes drag the magnetic field lines and twist the magnetic fields. Then the bipolar jets are collimated by the strong magnetic force with increasing azimuthal component of jets with the distance from the black hole.[1, 2]

2.3 High accuracy relativistic magnetohydrodynamics (HARM)

HARMPI is a parallel 3D version of high accuracy relativistic magnetohydrodynamics (HARM) with increased speed of the code and new features than HARM. The main difference between HARMPI and HARM is that HARMPI is parallelized using massage passing interface (MPI) and is fully operational in 3D. Since two codes share the same schema and follow the convention, here we explain in terms of HARM, which is also applicable to HARMPI. HARM solves hyperbolic partial differential equations, i.e., wave equation, using high-resolution shock-capturing technique, i.e., computing any shock waves or discontinuities of flows with zero viscosity. It was primarily written using GRMHD equations, and it can solve almost any set of hyperbolic equations in conservative

form:

$$\frac{\partial U}{\partial t} + \frac{\partial F(U)}{\partial x^i} = S(U) \tag{2.1}$$

where U, F, and S each represents conserved variables (mass, momentum, and energy), fluxes, and the sources, respectively. F can be calculated by solving $P(U) = U^{-1}(P)$ where $U(P)$ is a known set of equations in GRMHD and P is a primitive variable such as velocity and pressure. Most calculations performed in HARM are driven by calculations of P, i.e., MHD quantities including fluxes and sources can be derived from P. Similar to the original HARM code, HARMPI enables the use of non-uniform grids and solves the GRMHD equations to model the accretion disk and black hole dynamics in Kerr-Schild coordinates, one of the coordinates used to express the Kerr metric which describes the geometry of empty spacetime around a rotating, uncharged black hole [19, 20].

HARM is written in a conservative numerical scheme for a hyperbolic system. This choice guarantees to have the first-order hyperbolic partial differential equation converge towards a solution of the equations by the Lax-Wendroff theorem. Here, a solution implies a stable and consistent solution that does not blow up and is well-behaved numerically. Although the scheme is not guaranteed to work in the multidimensional flows, HARM assumes that it would be still applicable. The scheme also guarantees to satisfy the jump conditions at discontinuities in any number of dimensions, meaning that the code should not break down in examining different boundary conditions. Non-conservative schemes, on the other hand, with artificial viscosity do not guarantee these points and are also known to have troubles in relativistic shocks.

Many schemes have been adopted for the relativistic fluid dynamics and the simulations. What has not existed until recently is a scheme that includes magnetic fields, that has been fully verified

and convergence tested and is stable and capable of integrating a flow over many dynamical times. We chose HARMPI to simulate the Bondi accretion flows as well as the torus with jets, and the setups for each simulation is further explained in Chapter 3 and 4. The governing equations and the essential equations used in the project are described in the following section.

2.3.1 Governing equations

Fundamental equations used in HARM are (1) the particle number conservation equation, (2) the four energy-momentum equations, (3) the MHD stress-energy tensor equation, and (4) the induction equation that relates the velocity of conductive fluid and the magnetic field. These hyperbolic equations are written in a conservation form, i.e., spatially constant or fixed, in order to resolve any shock or discontinuity inside the equation or solution. We present the equations of GRMHD in the form used for the numerical integration in this section. In these equations, $c = 1$ and other notations follow the conventions. We focus on thermodynamical quantities such as internal energy, pressure, and density in order to compute certain outputs. This section mainly introduces the equations for these quantities.

The first set of equations describes the conservation of the particle number:

$$\nabla_\nu(\rho_0 u^u) = 0 \tag{2.2}$$

where ρ_0 is the rest-mass density, u^ν is the contravariant 4-velocity, and $\rho = \rho_0 u^t$ is the lab-frame mass density.

The second set of equations describes the energy-momentum conservation:

$$\nabla_\nu T^u_\nu = 0 \tag{2.3}$$

where the stress energy tensor T_v^u includes both matter (M) and electromagnetic (E) terms:

$$T^{M\mu}_{\ \ \nu} = (\rho_0 + u_g + p_g)u^\mu u_\nu + p_g\delta^\mu_\nu \tag{2.4}$$

$$T^{E\mu}_{\ \ \nu} = b^2 u^\mu u_\nu + p_b\delta^\mu_\nu - b^\mu b_{nu} \tag{2.5}$$

$$T^\mu_\nu = T^{M\mu}_{\ \ \nu} + T^{E\mu}_{\ \ \nu} \tag{2.6}$$

Here, the matter term (M) can be divided into a particle (P) term: $T^{P\mu}_{\ \ \nu} = \rho_0 u_\nu u^\mu$ and an enthalpy (EN) term. Both particle (P) and enthalpy (EN) terms make up for a free thermo-kinetic energy term (KE), which the matter term (M) can be further reduced to:

$$T^{MKE\mu}_{\ \ \nu} = T^{M\mu}_{\ \ \nu} - \rho_0 u^\mu \eta_\mu/\alpha \tag{2.7}$$

$$T^{PKE\mu}_{\ \ \nu} = (u_\nu - \eta_\nu/\alpha)\rho_0 u^\mu \tag{2.8}$$

$$T^{EN\mu}_{\ \ \nu} = (u_g + p_g)u^\mu u_\nu + p_g\delta^\mu_\nu \tag{2.9}$$

such that $T^{MKE\mu}_{\ \ \nu} = T^{PKE\mu}_{\ \ \nu} + T^{EN\mu}_{\ \ \nu}$. Here, u_g is the internal energy density, and $p_g = (\Gamma - 1)u_g$ is the ideal gas pressure with adiabatic index $\Gamma = 4/3$ or $\Gamma = 5/3$, which depends on the simulation types. The relation between the internal energy density and the ideal gas pressure is $u = \frac{p}{\Gamma - 1}$ [21]. These parameters are computed both numerically and analytically for the Bondi accretion flows simulation and described in Section 3.1.

2.3.2 Implementation

Some details are also provided by HARM in order to complete the implementation. HARM is written in a conservative scheme with second order in time (two derivatives with respect to time) by taking a half-step from t^n to $t^{n+1/2}$ or $U(t^n)$ to $U(t^{n+1})$ in computation. HARM also modifies the energy equation by subtracting an equation of the particle number conservation from the energy

equation in order to prevent inaccuracy caused by a direct implementation of the energy equation.

HARM further specifies geometric quantities as it would be difficult to accurately encode analytic expressions of all the quantities in every grid zone. It is coded to provide an analytic expression for $g_{\mu\nu}$, a metric tensor, and all other geometric quantities are calculated numerically at a high accuracy through numerical differentiation of the metric. This simplicity minimizes the risk of coding errors when specifying the geometric quantities and makes it relatively easy to change the coordinate systems according to the problems at hand.

Since negative densities and internal energies are not allowed by the GRMHD equations, HARM puts floor values for both parameters. HARM also sets up the outflow boundary conditions at the inner and outer radial boundaries in the rotating black hole [18]. Between the two versions (serial and parallel) available for the code, we chose the parallel version of the simulation and used Amazon Web Services (AWS). We used an AWS instance c6g.4xlarge with 16 CPUs and the storage of 30 GB is used for both simulations.

3. HARMPI simulation of Bondi accretion flows

3.1 Spherical accretion onto black holes

Accretion is the process when the compact objects gravitationally capture the ambient matter. Accretion of the gas onto compact objects is likely the source of energy for various astrophysical phenomena such as rapidly varying emission at a high luminosity of the compact regions within the quasars or the active galactic nuclei. Here, the supermassive black hole at the center of the object powers the system by accreting matter. When the matter falls through the steep gravitational potential, a significant fraction of the accreted rest-mass energy may be converted into radiation, which makes the process observable. Thus, accretion is a considerably more efficient cosmic energy source than many other commonly involved mechanisms in astrophysics such as nuclear fusion [22].

Bondi accretion is one of the accretion models, describing the accretion of a uniform fluid, i.e., interstellar gas, onto astrophysical objects. The relativistic extension of the model represents the accretion onto a black hole [23]. The accretion flow in the black hole system with speeds below the local speed of sound is subsonic at $r = \infty$ and with speeds above the local speed of sound is supersonic close to the black hole. Thus, as the radial velocity of the flow increases monotonically as the flow moves towards the black hole from infinity, the flow should pass a point where the

radial velocity is equal to the local speed of sound. This is a point where transition between subsonic and supersonic flow happens, which is known as a critical or sonic radius, r_s [24]. In this chapter, the general relativistic spherical, steady-state, and adiabatic accretion onto a rotating black hole is investigated. Furthermore, a sonic radius of the flow is determined both numerically and analytically using the relativistic Bondi equation.

3.2 Problem approach and simulation setups

We investigated a 1D Bondi accretion with HARMPI code. The goal of this investigation is to examine the changes of density over time as accretion is initiated from a spherical shell around the black holes and determine the sonic radius. The settings of the simulation and the physical parameters are described in this section. HARM and HARMPI share the same settings, so the explanation of the settings of the HARM code is interchangeable with HARMPI.

An analytic solution for Bondi accretion in the Schwarzschild geometry, spacetime that describes an empty space surrounding any spherical mass, is available and can be compared with the output of HARM. HARM fixes the sonic point $r_s = 8GM/c^2$, mass accretion rate $\dot{M} = 4\pi r^2 \rho u^r$, and an adiabatic index $\gamma = 4/3$ and integrates in the domain $r \in (1.9, 20)GM/c^2$ for $\nabla t = 100GM/c^3$. Note that the values here are not in physical units, and the units are going to be omitted. The coordinate is based on the Kerr-Schild system whose line element of

$$\begin{aligned} ds^2 = &-(1-2r/\rho^2)dt^2 + (4r/\rho^2)drdt + (1+2r/\rho^2)dr^2 + \rho^2 d\theta^2 + \\ &sin^2\theta(\rho^2 + a^2(1+2r/\rho^2)sin^2\theta)d\phi^2 \\ &-(4arsin^2\theta/\rho^2)dtd\phi - 2a(1+2r/\rho^2)sin^2\theta drd\phi \end{aligned} \tag{3.1}$$

and $GM = c = 1$. In (3.1), $\rho^2 = r^2 + a^2 cos\theta$, with $a/M = 0$ for this problem. Initial conditions and the physical parameters are listed in Table 3.1 below

Parameter	Values
a/M	0.9375
γ	4/3
r_{in}	10
t_{final}	200000.0

Table 3.1: Parameters of the Bondi simulation

where a/M, γ, r_{in}, and t_{final} each represents the spin parameter of the black hole, the adiabatic index, the radius of inner edge of the initial density distribution, and the run time of the simulation. The symbols used for the output variables are defined as $v1p$ for one of the characteristic velocities, ρ for the density, ug for the internal gas energy density, and pg for the gas thermal pressure.

The problems starts with a uniform density and temperature at $r = 10$. The density and pressure inside this radius is very low, and this region should be quickly accreted by the black hole. It simulates a spherically symmetric accretion from the ambient medium with a uniform density. Plotting the characteristic velocity would indicate the sonic radius of the infalling matter. This velocity should be greater than 0 when the flow barely falls inward compared to the fast, outgoing wave, while it should be less than 0 when the flow starts to fall inward supersonically near the black hole at the small radii. The radius at which the sign of this characteristic velocity changes over the time indicates the sonic radius.

3.3 Convergence study

Quantitative accuracy of the simulation result is important to support and consolidate the result of observational studies. The accuracy depends on both the appropriate physical model and the

artificial effects from the simulations. Spatial resolution is one of such important factors that easily vary the accuracy of the simulation results [24]. In this particular simulation, insufficiently low spatial resolution would lead the accretion flows to become more diffusive and cause the lower accretion rate and therefore affect the resultant output such as energy. Higher spatial resolution does not necessarily give a closer result to the exact solution as the solution should depend on the convergence rate and the accuracy of the physical model. The resolution should give the most accurate solution with the best efficiency, and the resolution of $(256 \times 1 \times 1)$ is suggested in HARM documentation for 1D Bondi simulation.

We perform a basic convergence study to demonstrate if a suggested resolution would give the result that is the closest to the analytical solution, i.e., sonic radius in this problem. A set of resolutions, $(128 \times 1 \times 1)$, $(256 \times 1 \times 1)$, and $(512 \times 1 \times 1)$, was tested with constant parameters throughout the test. Calculation and comparison of the sonic radius are extensively done in Section 3.5. In fact, the analytical solution of the sonic radius (all in gravitational radii) is ≈ 190.9 and the result in $(256 \times 1 \times 1)$ is ≈ 190.8 while the results in $(126 \times 1 \times 1)$ and $(512 \times 1 \times 1)$ are each ≈ 189.9 and ≈ 191.2. Thus, the suggested resolution of $(256 \times 1 \times 1)$ gave the closest solution to the analytical solution for the sonic radius. However, further studies should be done with the higher resolution of $(512 \times 1 \times 1)$ because the result is not similar to the analytical solution. This is further discussed in Chapter 5.

3.4 Results

This section provides the output and the results of the 1D Bondi problem. The first output is a 1D graph of the density of the ambient matter over the radius from the black hole. At the earlier times, the region inside $r = 10$ has $ug \approx 10^{-5}$ as the initial density for this region is set to be very low. Also, the density is shown to be uniform at the radius equal or greater than $r = 10$, $ug \approx 1$. Over the course of simulation, the region inside $r = 10$ quickly accretes and becomes denser with the turnoff radius, where the graph starts diverging, also increasing with the time. This implies that the closer the region is to the black hole, the ambient matter gets accreted quicker, resulting in the densest region. Increasing turnoff radius also implies that the density at larger radii starts increasing as more matter falls in.

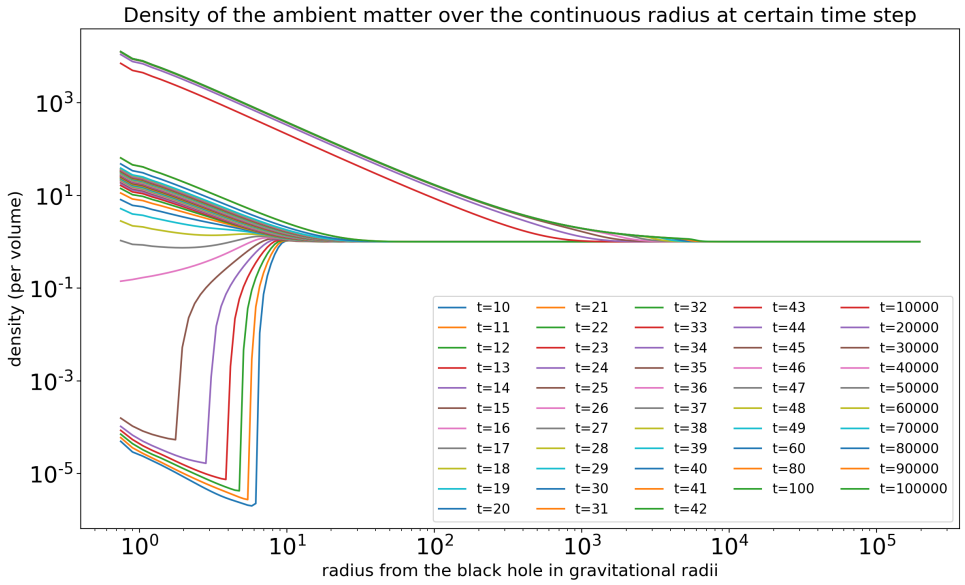

Figure 3.1: Density of the ambient matter at specific radii at a different time step

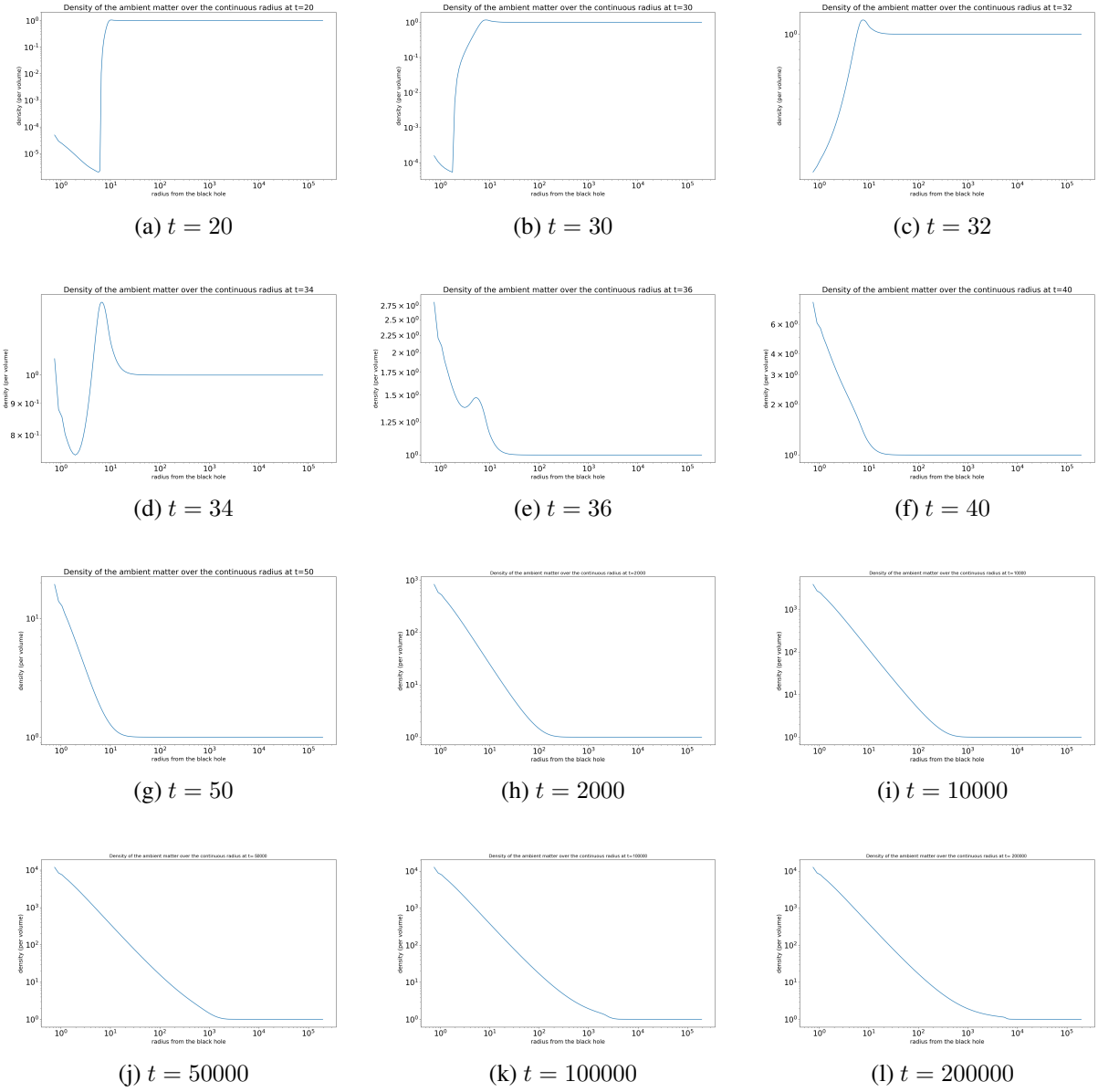

(a) $t = 20$ (b) $t = 30$ (c) $t = 32$

(d) $t = 34$ (e) $t = 36$ (f) $t = 40$

(g) $t = 50$ (h) $t = 2000$ (i) $t = 10000$

(j) $t = 50000$ (k) $t = 100000$ (l) $t = 200000$

Figure 3.2: The evolution of density throughout the time at specific time steps

Figure 3.2 contains 12 selected time steps to show the sequential behavior of the density. Narrower time steps at early time are chosen, while a larger time steps at later time are chosen because the rate at which the low density matter accretes at earlier times is much faster than the rate at which the turnoff point increases at the larger radii. Increase in the turnoff point can be found explicitly in these figures. Similarly, Figure 3.3 is a 1D graph of the internal gas energy density of

the matter. It represents the amount of energy stored in a given radius per unit volume. Therefore, the graphs of energy density are expected to show a similar manner in the graphs of density of the ambient matter. As mentioned in Section 3.1, there is a relationship between the accreted rest-

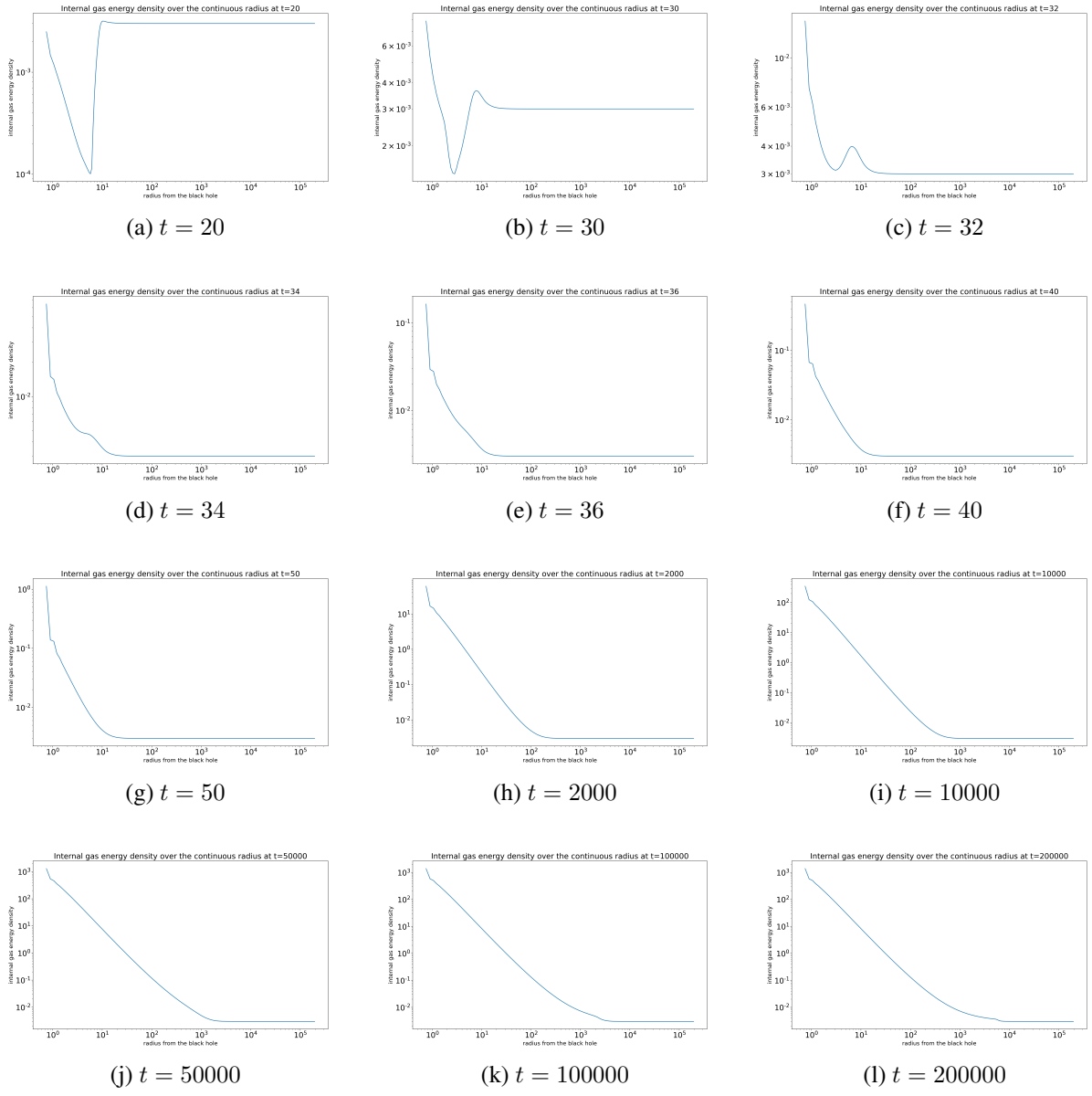

(a) $t = 20$ (b) $t = 30$ (c) $t = 32$

(d) $t = 34$ (e) $t = 36$ (f) $t = 40$

(g) $t = 50$ (h) $t = 2000$ (i) $t = 10000$

(j) $t = 50000$ (k) $t = 100000$ (l) $t = 200000$

Figure 3.3: The evolution of the internal gas energy density at specific time steps

mass energy and the radiation. The rest-mass energy increases over time as more ambient matters accrete. As more ambient matters accrete, the density and energy density increase. Indeed, the

Figure 3.3 is analogous to Figure 3.2, showing a faster rate for the inner region being filled out and an increment in turnoff radius at later times. Figure 3.4 is a 1D graph of the thermal gas pressure of the matter. The way it is calculated has a factor of the energy density as introduced in Section 2.3.1 and only depends on the adiabatic index, which is kept constant throughout the simulations. The graphs at chosen time steps are presented in Figure 3.4.

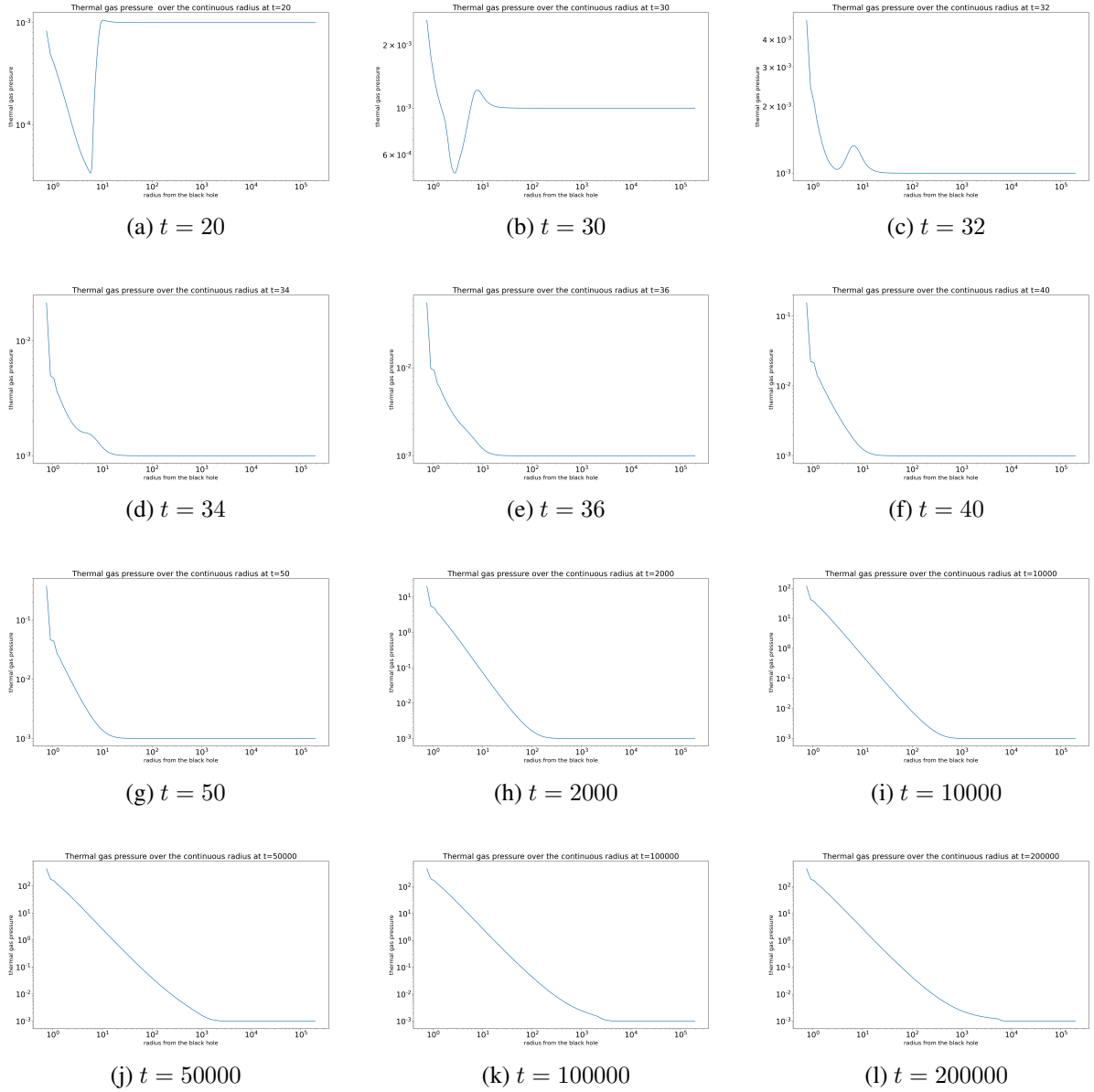

(a) $t = 20$ (b) $t = 30$ (c) $t = 32$

(d) $t = 34$ (e) $t = 36$ (f) $t = 40$

(g) $t = 50$ (h) $t = 2000$ (i) $t = 10000$

(j) $t = 50000$ (k) $t = 100000$ (l) $t = 200000$

Figure 3.4: The evolution of the thermal gas pressure at specific time steps

3.5 Sonic radius

3.5.1 Analytical solution

The analytical solution of the sonic radius is available. The relativistic equation of the sonic radius is listed in the Appendix G from the book, *Black holes, white dwarfs, and neutron stars: The physics of compact objects*. For the simplicity, we show a derivation of a non-relativistic equation of the sonic radius below. This equation is taken from the textbook *Radiative gas dynamics, Chapter 8. Spherical accretion.*

We start by the equation of momentum conservation (Eqn 3.2) and the equation of mass conservation (Eqn 3.3).

$$u\frac{du}{dr} + \frac{a^2}{\rho}\frac{d\rho}{dr} + \frac{GM}{r^2} = 0 \tag{3.2}$$

$$\frac{1}{\rho}\frac{d\rho}{dr} = -\frac{2}{r} - \frac{1}{u}\frac{du}{dr} \tag{3.3}$$

Combining these two equations, we get an equation called the Bondi equation (Eqn 3.4).

$$\frac{1}{2}\left(1 - \frac{a^2}{u^2}\right)\frac{d}{dr}(u^2) = -\frac{GM}{r^2}\left[1 - \frac{2a^2 r}{GM}\right] \tag{3.4}$$

Let us assume that there is a radius r_s that makes both right and left terms vanish, which means that the solutions should be either in a form of Eqn 3.5 or Eqn (3.6).

$$u(r_s)^2 = a(r_s)^2 \tag{3.5}$$

$$\frac{d(u^2)}{dr}|_{r=r_s} = 0 \tag{3.6}$$

There are six types of solutions to the Bondi equation, classified by the behavior of the flow at r_s. The types are shown in Figure 3.5 below. Here, we focus on the solution (1), a transonic solution where r_s is a sonic radius, in order to determine the accretion rate in terms of the mass of the accreting matter, the density at infinity, and the sound speed at infinity.

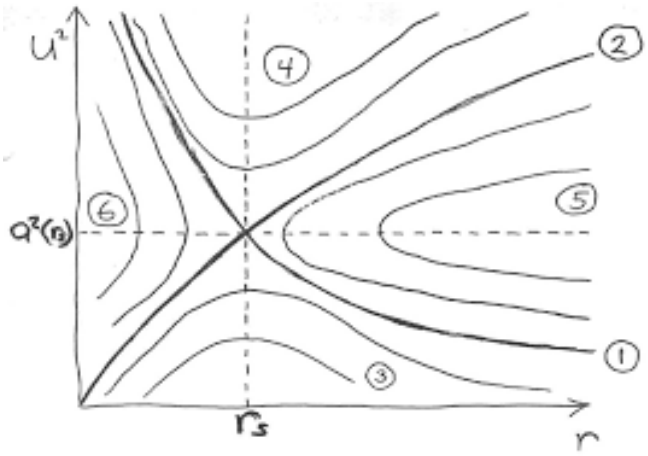

Figure 3.5: Solutions of the Bondi equation. We focus on solution type 1.

The equation of momentum conservation (Eqn 3.2) can be integrated and yield (Eqn 3.7), which is known as the Bernoulli integral.

$$a(r_s)^2 \left(\frac{1}{2} + \frac{1}{\gamma - 1} - 2 \right) = \frac{a_\infty^2}{\gamma - 1} \tag{3.7}$$

This equation further implies that

$$r_s = \frac{5 - 3\gamma}{4} \frac{GM}{a_\infty^2} \tag{3.8}$$

which is a non-relativistic equation for the sonic radius. Since our case of accretion has a relativistic effect, we use relativistic velocity equation (Eqn 3.9) and sound speed equation (Eqn 3.11) to derive

a relativistic equation for the sonic radius.

$$u_s^2 = \frac{a_s^2}{q + 3a_s^2} = \frac{1}{2r_s} \tag{3.9}$$

$$\therefore a_s^2 = \frac{1}{2r_s - 3} \tag{3.10}$$

Then we plug $a_\infty = (\gamma P_\infty / \rho_\infty)^{1/2}$ and Eqn 3.10 into Eqn 3.12, which is derived from the relativistic Bernoulli equation.

$$\left(1 + 3a_s^2\right)\left(1 - \frac{a_s^2}{\gamma - 1}\right)^2 = \left(1 - \frac{a_\infty^2}{\gamma - 1}\right)^2 \tag{3.11}$$

$$\left(1 + \frac{3}{2r_s - 3}\right)\left(1 - \frac{1}{(2r_s - 3)(\gamma - 1)}\right)^2 = \left(1 - \frac{a_\infty^2}{\gamma - 1}\right)^2 \tag{3.12}$$

$$\left(1 + \frac{3}{2r_s - 3}\right)\left(1 - \frac{3}{2r_s - 3}\right)^2 = \left(1 - \frac{1}{4 \times 10^{-3}}\right)^2 \tag{3.13}$$

The values for ρ_∞, P_∞, and γ are all given in the previous sections. Assuming that $r = 200000$ is enough to approximate these values estimated at infinity, each value corresponds to $10^0 = 1$, 10^{-3}, and $4/3$. The solutions to Eqn 3.13 are $r_s \approx -0.9\ldots$, $r_s \approx 2.4\ldots$, and $r_s \approx 190.8\ldots$. Here, we discard the first solution with a negative value and the second solution with relatively small value. The infall of the matter reaches a steady state, implying that the third solution is a sonic radius. This value is compared with the result of the simulation in the following section.

3.5.2 Numerical solution

The sonic radius from the result of the simulation is estimated by solving the radius where the sign of the characteristic velocity, $v1p$, changes. As expected, the sonic radius approaches to a steady state after a sharp decline. It approaches and starts settling down at $r_s \approx 190.8$.

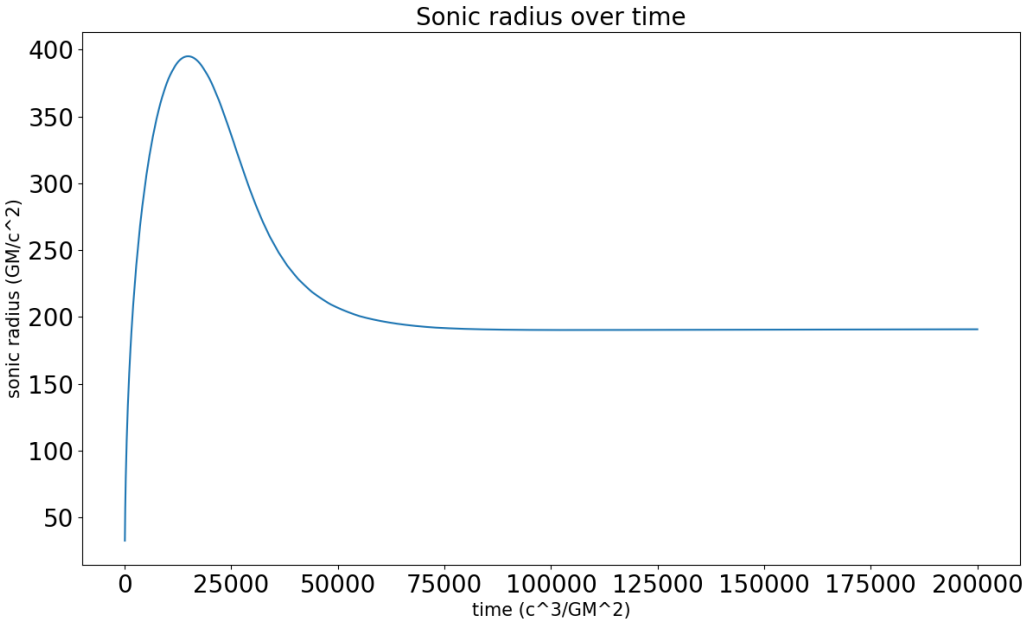

Figure 3.6: Sonic radius measured by the radius at which $v1p$ changes its sign

The discrepancy between the analytical and the numerical solutions may be caused by the insufficient time range or the radius range to be treated as r_∞. We confirmed that the numerical solution is a reasonable value that falls in the range of accuracy.

3.6 Physical implications

The Bondi model is used to estimate the sonic radius, or accretion radius which the matter starts to fall supersonically onto the black hole, and the mass accretion rate. It also allows estimating the mass of the accreted materials onto the black hole through the density and the velocity at the boundary conditions (at r_∞). It is found that a collisionless, weak-interacting fluid such as dark matter particles or halos also have the sonic radius that is analogous to that of Bondi model, which lies outside the event horizon [25]. Models of isolated galaxy have been developed by V. Springel

et al. (2005) and estimated that the growth of a small seed black hole accelerates at the same rate estimated by Bondi accretion model [26].

4. HARMPI simulation of torus and jets

4.1 Spin of a black hole

Astrophysical black holes are classified by two properties, mass and angular momentum, neglecting the charge as the universe is electrically neutral. Black holes that are formed from gravitational collapse have nonzero angular momentum, or spin, following conservation of angular momentum. They may gain more angular momentum from other black holes or the accreted materials in general [27]. Black hole spin is affected by the dynamics of the initial collapse and the angular profile of the progenitor star with further details on its mass, metallicity, and the magnetic field [28]. Depending on the spin, energy also can be extracted from rotating black holes via the Penrose process that describes how the black holes can take up one decayed particle's negative energy and momentum and transfer to the other decayed particle leaving the black holes. It specifies that up to 29 percent of such mass-energy can be extracted from a maximally rotating black hole [29]. Such extracted energy is assumed to be transported to the magnetic field, making a relativistic jet.

The spin is measured from the innermost stable circular orbit (ISCO) as the ISCO radius depends on the direction and the magnitude of the spin (Figure 4.1) [3]. Rotating black holes distort the spacetime metric around them, known as the frame-dragging effect, and make the nearby matter and light also rotate around the black holes. This is because the geodesic, or the shortest path

on the curved spacetime, of the matter and light is forced to follow the rotation of the black hole [30, 31]. This effect causes the ISCO radius to move either closer to or farther out from the black holes and therefore allows the measurement of the ISCO radius and the corresponding spin.

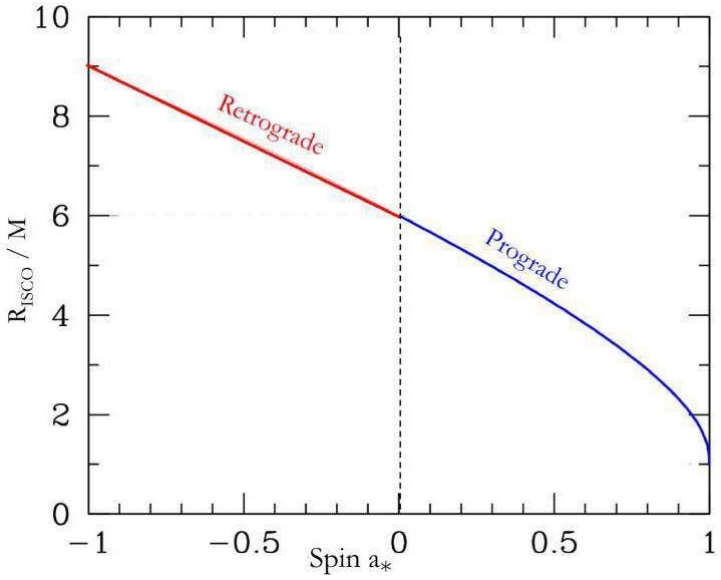

Figure 4.1: The relation between the ISCO radius and the black hole spin [3]

The ISCO radius specifically represents the location where the relativistic effects near black holes destabilize the circular orbit of the matter and light and cause them to spiral into the event horizon. If a black hole and the accretion disk rotate in a same direction (prograde, positive spin), ISCO radius moves much closer to the black hole as it has higher spins [30]. For a non-rotating black hole with $a/M = 0$, the ISCO radius is at $6M$. If a black hole and the accretion disk rotate in an opposite direction (retrograde, negative spin), ISCO radius moves farther out from the black hole as it has higher spins in magnitude. In the prograde regime, the accretion efficiency, which refers to the change of relativistic energy per unit mass of a particle falling from the rest at infinity, increases as the angular momentum increases, up to $0.42\dot{M}c^2$ where $\dot{M}$ is the accretion rate onto a black hole. As the spin decreases to 0, the accretion efficiency drops as well, reaching $0.06\dot{M}c^2$,

as the ISCO locates farther away from the black hole. In the retrograde regime, the accretion efficiency is lower than that of the zero spin because the ISCO moves much farther outwards [32]. The accretion efficiency can be further converted into the mechanical energy such as winds and jets or thermal and radiative energy.

The spin is mathematically defined as a dimensionless quantity, $a = Jc/GM^2$ where M is the mass of a rotating black hole, J is the angular momentum, c is the speed of light, and G is the gravitational constant, and must range from -1 to 1 [28]. The equation for a black hole's event horizon radius is given as $r_e = M + (M^2 - a^2)^{1/2}$, and when $a/M = 0$, i.e., zero spin, this radius simply reduces to Schwarzschild radius, i.e., a radius of a non rotating black hole. If $a/M > 1$, then there is no horizon, and the rotating black hole hypothetically becomes naked singularity, meaning the singularity is not surrounded by the horizon [33]. The maximum possible spin is one of the fundamental questions yet to be solved. Thorne (1974) suggested that $a/M = 0.998$ is a maximum spin because the black hole may lose its angular momentum from the negative angular momentum as the accreted materials may flow back from the black hole to the disk if the magnetic field is strong. A number of studies have suggested that this maximum limit may be higher or lower than this value, depending on the type of flow and the geometry [27]. In fact, GRS 1915+105, a microquasar (a galactic jet source similar to quasar with stellar-scaled jets), has been observed with a spin of $a/M = 0.98 \pm 0.01$, and Cygnus X-1, a black hole X-ray binary, has been observed with a spin of $a/M = 0.9985$ [34, 35].

4.2 Problem approach and simulation setups

In this chapter, we simulate a torus around a black hole to investigate the effect of the spin on the accretion rate and the power output of a magnetized jet. We used GRMHD code HARMPI for the simulations. HARM and HARMPI use the same parameters and follow the convention.

HARM sets initial conditions to have a rotating torus of fluid held together by gravity, pressure, and centrifugal forces. The values of mass accretion rate and the energy at the initial boundary are small because the initial conditions are set to be unstable. The magnetorotational instability develops after the magnetic field reaches sufficient strength to twist the torus and drop the materials onto the black hole. Torus becomes turbulent, allowing the black hole to accrete materials at the steady state [36, 18]. Turbulence and the accretion flow continue throughout the simulation.

HARM simulates a torus in a hydrostatic equilibrium, which is analogous to the stable donut-shaped plasma that is embedded in vacuum and surrounds a black hole. Centrifugal forces and pressure support this torus. The simulation is based on the solutions of Fishbone and Moncrief, a simple model of a magnetized torus, which is developed to keep the solutions analytical [28]. Fishbone-Moncrief torus is a model of ideal fluid disk around the black holes, simply assuming that the fluid is stationary, axisymmetric, purely azimuthal in an arbitrary, stationary, axisymmetric gravitational field. We study the structure of those fluid disks around the rotating black holes with constant angular momentum [37].

The astrophysical problem here is the evolution of a magnetized torus near a rotating black hole. The simulation contains Fishbone-Moncrief torus with an inner radius at $r = 6M$ and maximum pressure at $r = 12M$. Similarly $GM = c = 1$ applies here. The initial magnetic

field is purely poloidal, and the magnetic field is derived from a vector potential and is limited to have a minimum ratio of gas to magnetic pressure of 100. At the inner boundary, the magnetic field strength is parameterized by b^2/ρ, where b is a magnetic field four-vector. The numerical resolution of $(256 \times 256 \times 1)$ has chosen, with the computational domain at $r_{in} = 0.8r_e$ where r_e is the event horizon radius. The inner boundary is inside the event horizon and therefore is isolated from the rest of the flow. Outer boundary of the computational domain is at $r_{out} = 40M$. Fiducial tests suggest that the results are independent from r_{in} and r_{out}, and the outer boundary has negligible influence on the inner accretion flow [18]. The simulation was run up to $t = 10000c^3/GM$. The spin parameters of $a/M \in (0.0, 0.1, 0.2, 0.3, 0.4, 0.5, 0.6, 0.7, 0.8, 0.9, 0.95, 0.98)$ are chosen to draw a well distributed set of results.

4.3 Results

This section provides results of the torus simulation. The main result is a 2D graph with z-plane on the y-axis, radius from the black hole on the x-axis, and with the bar on the right side that represents the density. The 2D graphs from $t = 0$ to $t = 10000$ with an interval of $t = 200$ are created for each spin parameter and are displayed below in Figure 4.2 ($a/M = 0.1$) and 4.3 ($a/M = 0.98$). Note that the rest of the graphs are displayed in Appendix A. As expected, the matter starts to accrete in the faster rate at a higher spin parameter with a decreasing radius of the event horizon. The range of angles at which the matter enters the black hole also increases at a faster rate with the higher spin parameter.

After each simulation, we calculated the total accreted mass and the energy output.

$$\dot{M} = \int \int_{Area} uu\,[1] \times \rho \tag{4.1}$$

$$E = \int \int_{Area} (-gdet * Tud[1,0] \times \_dx2 \times \_dx3) \tag{4.2}$$

Eqn 4.1 is a mass flow rate equation, where $uu[1]$ is contravariant velocity in the radial direction and ρ is density. As $\dot{M}$ is calculated at each grid (1×1), values at each ϕ direction are summed over the simulation window to get the total mass accretion rate. Similarly, Eqn 4.2, where $gdet$ is a square root of the negative of metric determinant and $Tud[1,0]$ is the energy component of the stress-energy tensor, computes the energy at each grid. Summing all of these values at ϕ direction over the simulation window, we calculated the final energy output. The results are listed in Table 4.1, and note that these values are not in physical units.

Spin Parameter	Sum of Mass Accretion	Sum of Energy Output
a = 0	-4200	-2100
a = 0.1	-6300	-2900
a = 0.2	-7600	-3200
a = 0.3	-7700	-2700
a = 0.4	-6600	-910
a = 0.5	-6200	560
a = 0.6	-5000	3400
a = 0.7	-7100	3000
a = 0.8	-6900	5200
a = 0.9	-6600	7200
a = 0.95	-8800	8800
a = 0.98	-7400	8800

Table 4.1: Mass accretion rate and the energy output at different spin parameter. Note that the units are not physical units.

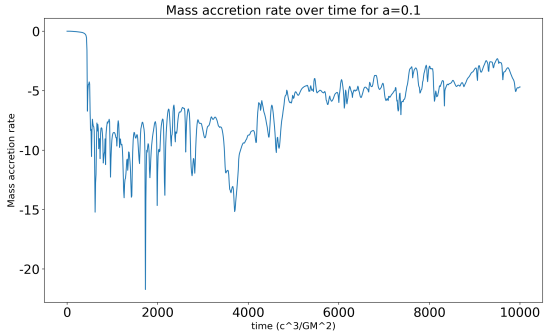

(a) Accretion rate of $a/M = 0.1$ over time

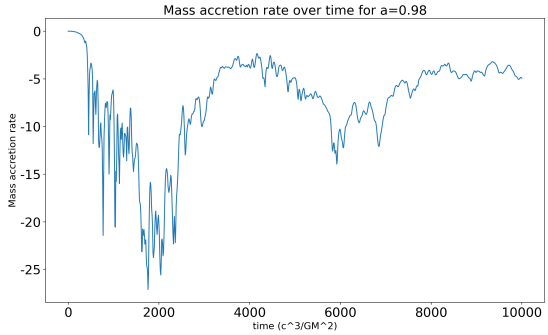

(b) Accretion rate of $a/M = 0.98$ over time

Figure 4.2: Accretion rate of the black holes with $a/M = 0.1$ and $a/M = 0.98$ over time

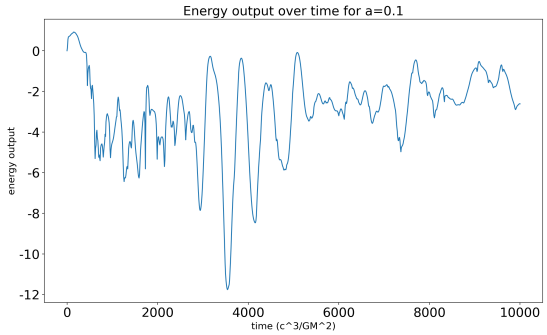

(a) Energy output of $a/M = 0.1$ over time

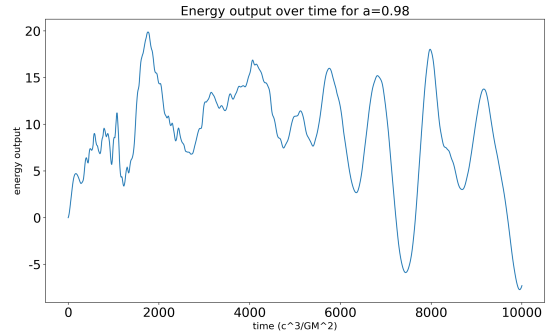

(b) Energy output of $a/M = 0.98$ over time

Figure 4.3: Energy output of the black holes with $a/M = 0.1$ and $a/M = 0.98$ over time

In Figure 4.2, accretion might develop in association with the turbulence driven by the magnetorotational instability. This turbulence seems to affect the accretion rate as we would expect because the turbulence prevents some of the ambient matter to fall into the black hole. The effect of turbulence is more notable at earlier times and becomes more stable at later times, which agrees with Figure 4.4 and Figure 4.5. A quasi-periodic signal is shown at later times in Figure 4.3. However, the reason for this signal is unclear (See Chapter 5 for the future works).

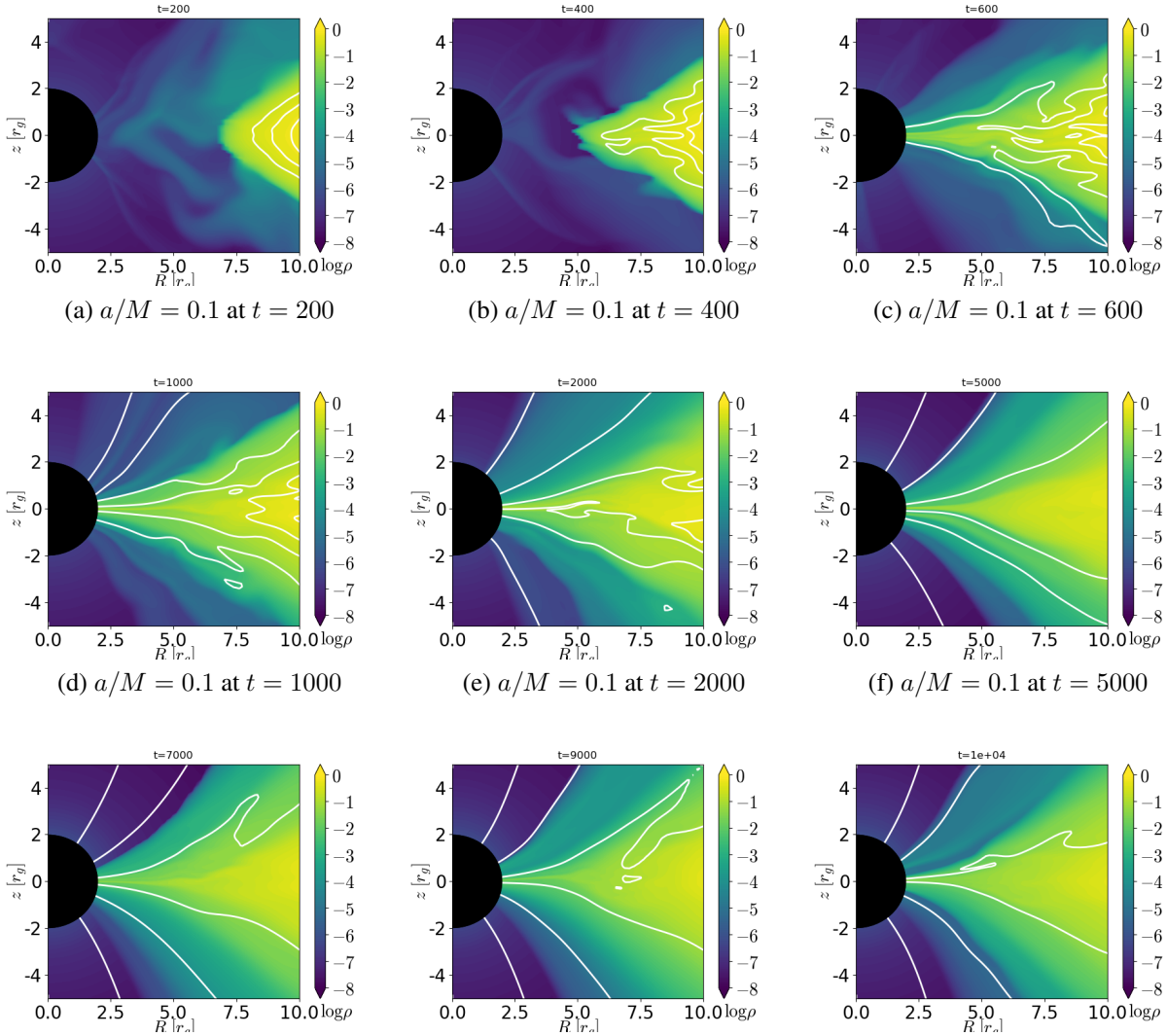

(a) $a/M = 0.1$ at $t = 200$ (b) $a/M = 0.1$ at $t = 400$ (c) $a/M = 0.1$ at $t = 600$

(d) $a/M = 0.1$ at $t = 1000$ (e) $a/M = 0.1$ at $t = 2000$ (f) $a/M = 0.1$ at $t = 5000$

(g) $a/M = 0.1$ at $t = 7000$ (h) $a/M = 0.1$ at $t = 9000$ (i) $a/M = 0.1$ at $t = 10000$

Figure 4.4: Evolution of a torus with $a/M = 0.1$ over the time. The white contours are magnetic field lines. The radius of the event horizon is greater and the angle at which the matter accretes is smaller than the Figure 4.4.

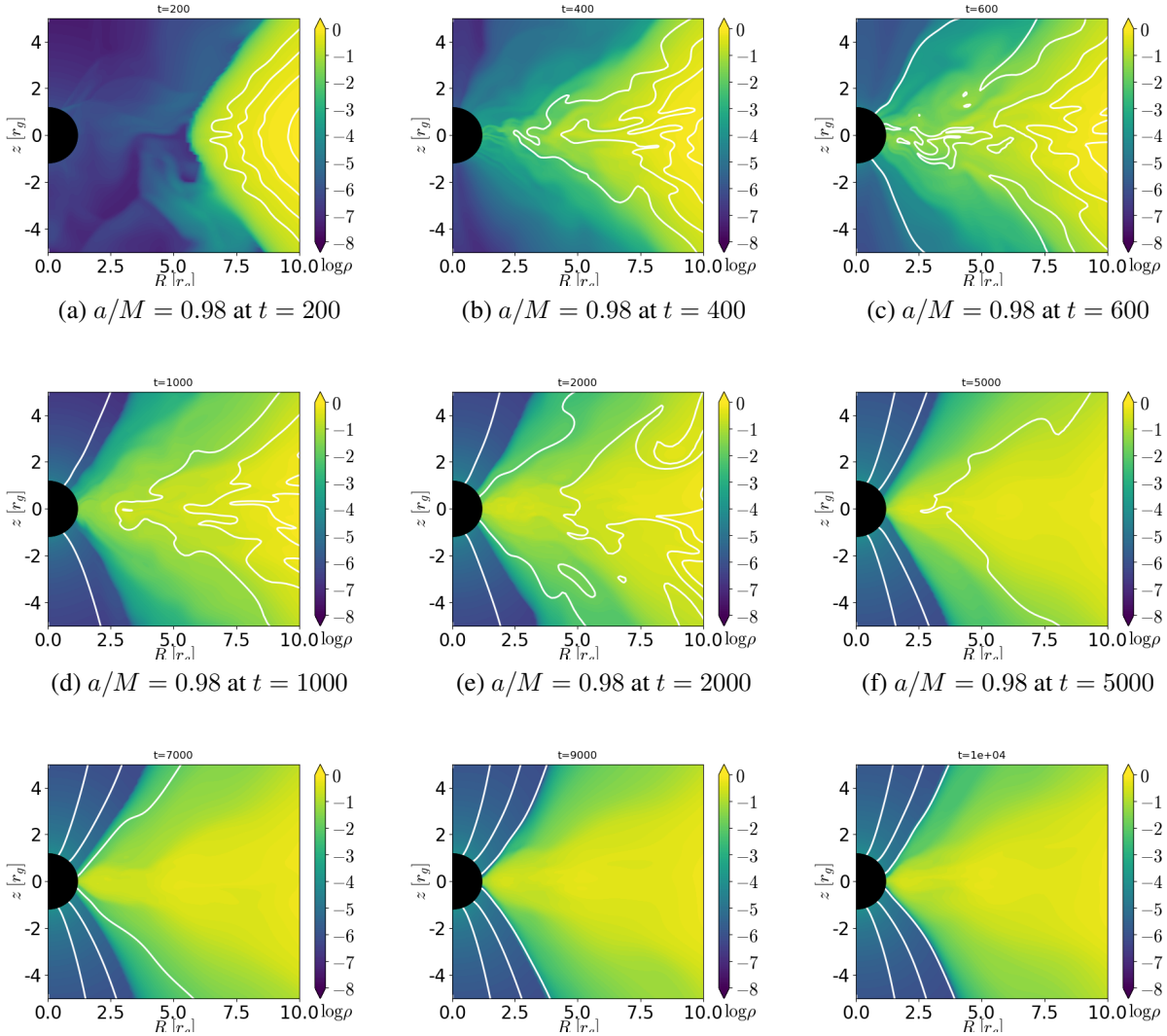

(a) $a/M = 0.98$ at $t = 200$ (b) $a/M = 0.98$ at $t = 400$ (c) $a/M = 0.98$ at $t = 600$

(d) $a/M = 0.98$ at $t = 1000$ (e) $a/M = 0.98$ at $t = 2000$ (f) $a/M = 0.98$ at $t = 5000$

(g) $a/M = 0.98$ at $t = 7000$ (h) $a/M = 0.98$ at $t = 9000$ (i) $a/M = 0.98$ at $t = 10000$

Figure 4.5: Evolution of a torus with $a/M = 0.98$ over the time. The white contours are magnetic field lines. The radius of the event horizon is much smaller, and the angle at which the matter accretes is greater than the Figure 4.3.

The results also show the relationships between the spin, mass accretion rate, and the energy. As shown in Table 4.1 and Figure 4.4, there is a positive trend between the spin and the energy. However, it does not seem to have any clear trend between the spin and mass accretion rate. Thus, the energy is correlated to the spin while the mass accretion does not appear to be. From our results, the mass accretion rate is always negative since the matter flows into the black hole from larger radii. The energy output increases from negative values at lower spin to the positive values at higher spin. This implies that the window of the simulation might be too small to compute the entire energy output at the lower spins. Furthermore, the negative energy outputs might point at a computational error as we would not expect the energy to be negative. In this scenario, running a simulation in a finer spatial resolution with a longer time window could be a future study.

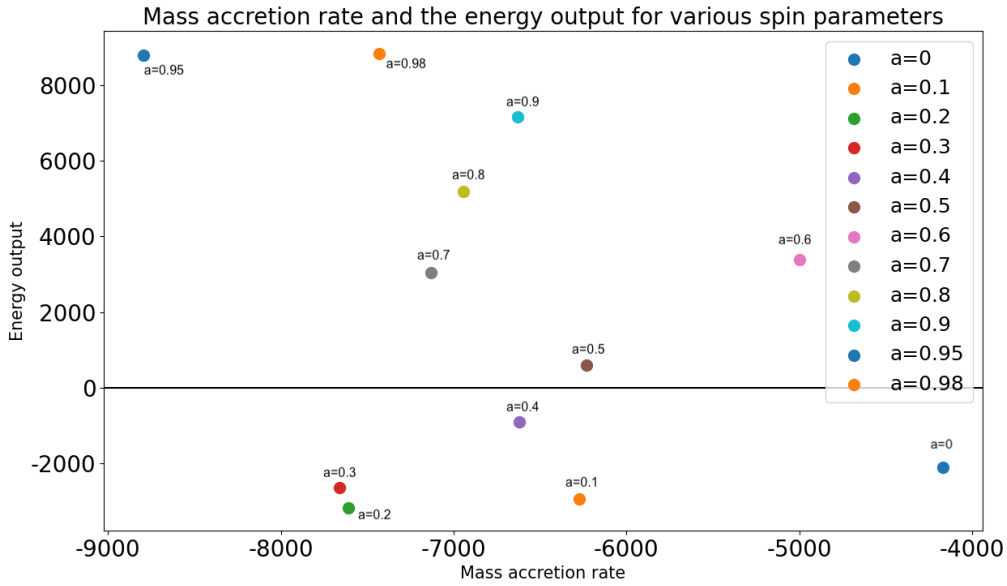

Figure 4.6: Sum of the total mass accretion rate and energy output for different spin parameters

Figures at $t = 2000$, $t = 6000$, and $t = 10000$ are further created with the mass accretion rate on x-axis and the energy output at y-axis for different spins. These figures show that the data

points randomly move around the plot over time and therefore does not show a clear relationship between the spin parameters and the mass accretion rates over the course of the simulations.

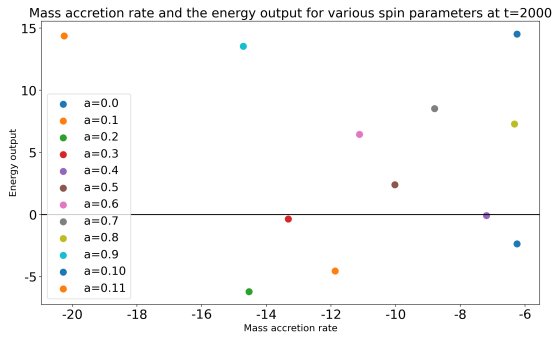

(a) $t = 2000$

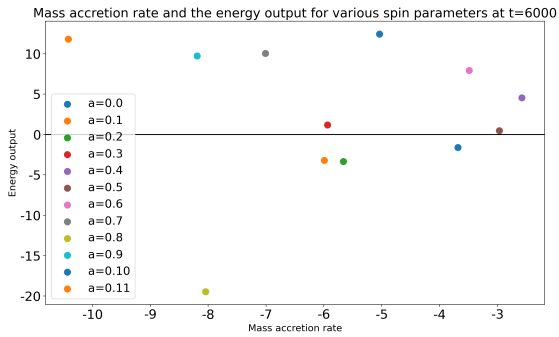

(b) $t = 6000$

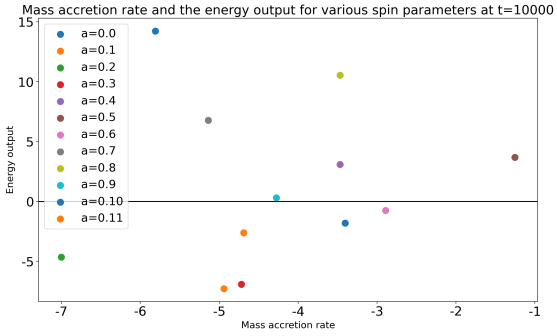

(c) $t = 10000$

Figure 4.7: Mass accretion rate and energy output for different spin parameters at certain time steps

4.4 Comparison to observational studies

One observational study of the galaxies using Chandra X-ray telescope [38] shows a relation between the Bondi accretion rate and the jet power. As shown in Figure 4.5, they modeled a linear relationship between the accretion power P_{Bondi} with the jet power P_{jet}. Here, P_{Bondi} is a different quantity from any quantity introduced in Chapter 3. They described the correlation with a

power-law model of the form

$$log\frac{P_{Bondi}}{10^{43}ergs^{-1}} = A + Blog\frac{P_{jet}}{10^{43}ergs^{-}1} \tag{4.3}$$

where $A = 0.67 \pm 0.07$ and $B = 0.74 \pm 0.08$ using $\tilde{\chi}^2$ fit statistic. They measured the galaxy velocity dispersion to find the central black hole mass and used X-ray luminosity to estimate the accretion rates onto the black holes. They also assumed that the Bondi type of accretion was happening to infer an accretion power from their observations, which turned out to be a reasonable assummption due to a tight correlation between P_{Bondi} and P_{jet}.

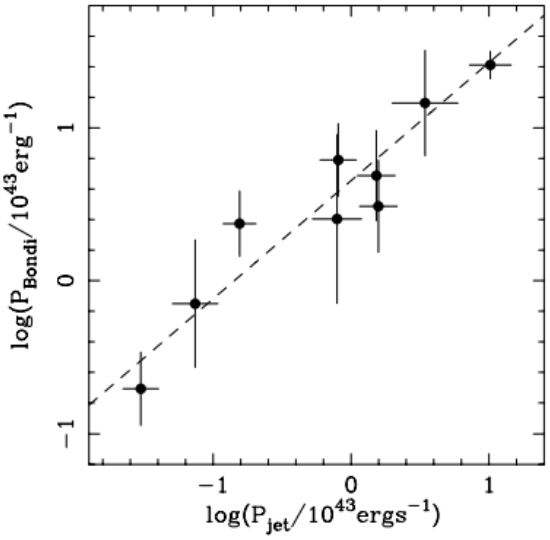

Figure 4.8: The relationship between the Bondi accretion power determined from Chandra X-ray data and the jet power. The dashed line is the best-fitting linear model.

5. Discussion

In this project, we studied Bondi accretion onto a rotating black hole and the evolution of the torus with jets as black hole accretes. We used HARMPI, code for the 3D general relativistic magneto-hydrodynamic simulations, to understand the dynamics of black holes and jets. The summary of the simulations and the directions for future study are introduced in this section.

We investigated the dynamic of a black hole through the change of density, pressure, and energy density of the ambient matter under a spherically symmetric accretion. We ran the simulations over time up to $t = 200,000$ and radius up to 10^5 gravitational radii. Parameters and the equations used in the simulations are explained in Section 3.2. We also performed a convergence study for Bondi 1D simulation. Three sets of a resolution are tested, $(126 \times 1 \times 1)$, $(256 \times 1 \times 1)$, a resolution suggested by HARM, and $(512 \times 1 \times 1)$. The simulation with a resolution of $(256 \times 1 \times 1)$ gave a solution of the sonic radius that is closest to the analytically calculated value, and therefore we confirmed the suggestion by HARM. We also determined the sonic radius analytically using the results of density and pressure from the simulations and the relativistic equations provided by and Shapiro and Teukolsky. Figure 3.5 is a graph with the sonic radius over time and shows that it approaches a steady state after a sharp decline. This steady point and the analytical solution are each ≈ 190.8 and ≈ 190.8, and we concluded that these two solutions reasonably match each other.

We suggest to re-perform the convergence tests done by the HARM team as a future work because the highest resolution tested in our convergence test, $(512 \times 1 \times 1)$, does not provide either a similar or much diverging result from the actual solution. Also, future work should include a further investigation of the relationship between different black hole spins and the location of the sonic radius. The relationship between the metallicity, the adiabatic index, and the sound speed may be interesting to explore as the metallicity affects the local sound speed, which should affect the sonic radius.

We also studied the effects of the black hole spin on the mass accretion rate and the energy of black holes. The HARM-suggested resolution of $(256 \times 256 \times 1)$ was used to run the simulation up to $t = 10,000$. Spin parameters of 0.0, 0.1, 0.2, 0.3, 0.4, 0.5, 0.6, 0.7, 0.8, 0.9, 0.95, and 0.98 were tested. Explanation for the parameters used in these simulations is provided in Section 4.2. The mass accretion rate and energy were computed for each spin parameter by summing all the fractional mass accretion rate and energy at each resolution grid over time. Table 4.1 summarizes the results for each spin parameter. A clear positive trend is found between the energy output and the spin parameter, i.e., as the spin of the black hole increases the energy released from the black hole increases. However, the mass accretion rate and the spin parameter do not seem to have a clear relationship as the mass accretion rate for each spin parameter tends to fluctuate over time. Previous observational study by S. W. Allen et al. [7] has shown a tight correlation between Bondi accretion rate and the jet power. Therefore, we suggest that the relationship between the spin parameter and the accretion rate should be further studied as both seem to be positively correlated to the energy output.

Note that the map of energy output over time (Figure A.12) shows a possibly periodic signal. This suggests a further study on the energy of the black holes. Since astrophysical black holes can

turn on and off the jets, whether the energy outflows have a periodic pattern or are affected by the periodic oscillation in the variability of the objects remain interesting studies. Another extensive study would be including the effects of magnetic field strength on both mass accretion rate and the energy as jet collimation and acceleration depend on the magnetic field around the black hole.

Our results have implications for understanding the nature of accretion and other astrophysical phenomena. In this study, we explored Bondi accretion onto a Kerr black hole over time, including tracking the sonic radius, which may help to understand the spherical accretion of black holes in gas-rich environments such as black hole seeds in the early universe. We also studied disk accretion and jet production in a magnetized disk around black holes of varying spins. We found a slight correlation of spin with energy output, and no clear relation between mass accretion rate and power output. Finally, We suggest to include testing the limits of the simulations, i.e., longer times and higher or better resolution, and exploring further dependence on magnetic field strength and retrograde disks as future studies.

A. Appendix

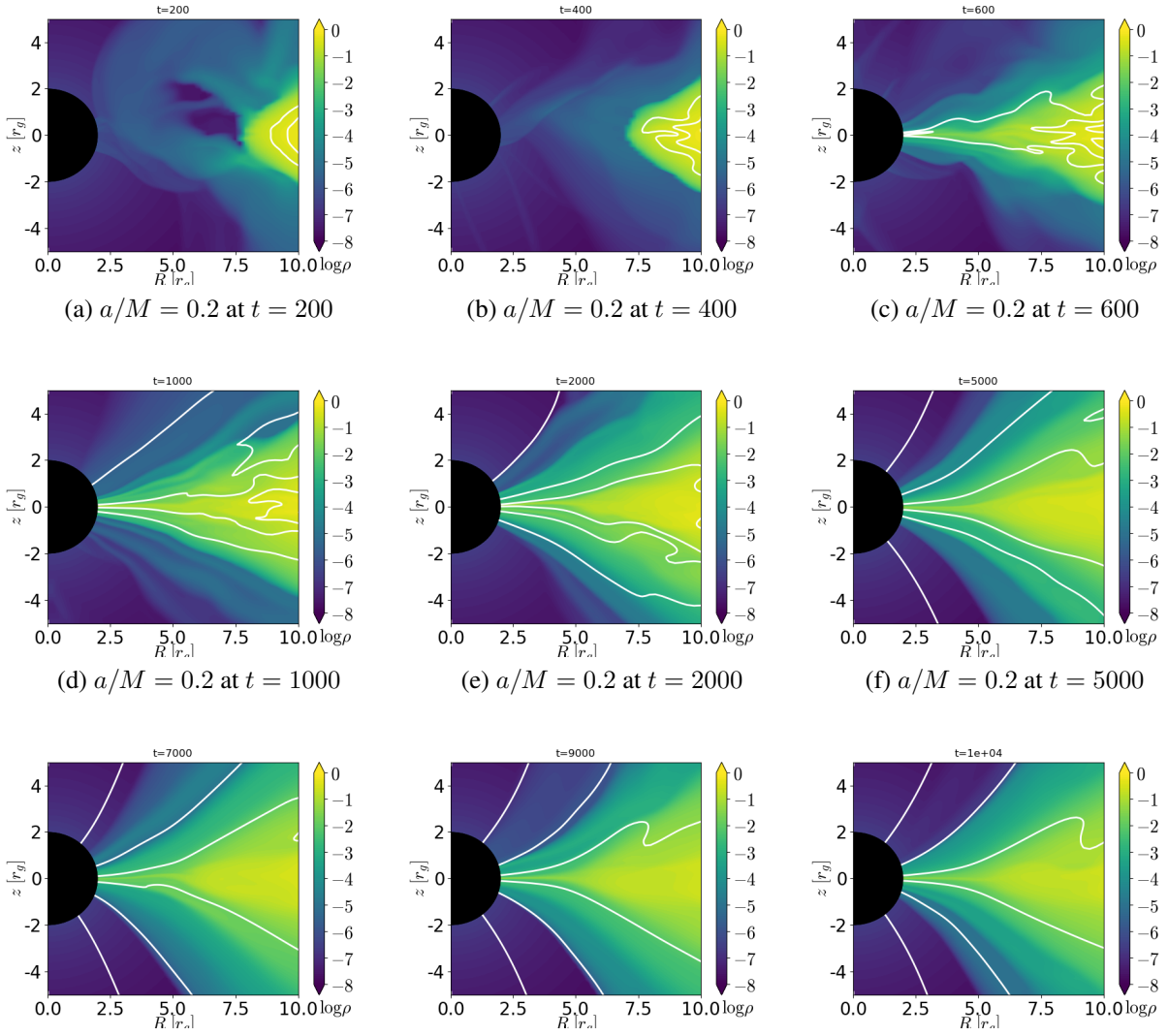

(a) $a/M = 0.2$ at $t = 200$ (b) $a/M = 0.2$ at $t = 400$ (c) $a/M = 0.2$ at $t = 600$

(d) $a/M = 0.2$ at $t = 1000$ (e) $a/M = 0.2$ at $t = 2000$ (f) $a/M = 0.2$ at $t = 5000$

(g) $a/M = 0.2$ at $t = 7000$ (h) $a/M = 0.2$ at $t = 9000$ (i) $a/M = 0.2$ at $t = 10000$

Figure A.1: Evolution of a torus with $a/M = 0$ at certain time steps

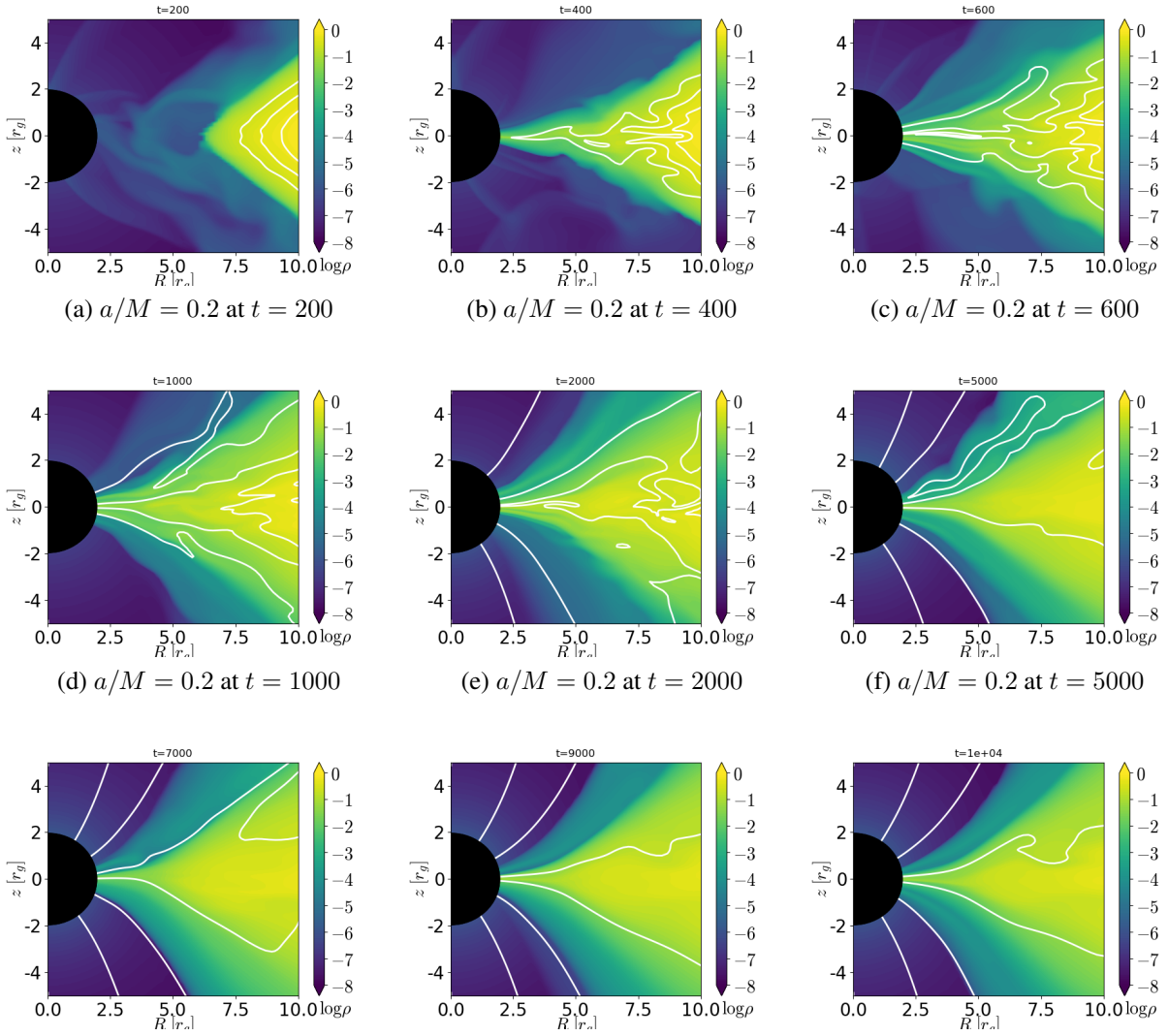

(a) $a/M = 0.2$ at $t = 200$ (b) $a/M = 0.2$ at $t = 400$ (c) $a/M = 0.2$ at $t = 600$

(d) $a/M = 0.2$ at $t = 1000$ (e) $a/M = 0.2$ at $t = 2000$ (f) $a/M = 0.2$ at $t = 5000$

(g) $a/M = 0.2$ at $t = 7000$ (h) $a/M = 0.2$ at $t = 9000$ (i) $a/M = 0.2$ at $t = 10000$

Figure A.2: Evolution of a torus with $a/M = 0.2$ at certain time steps

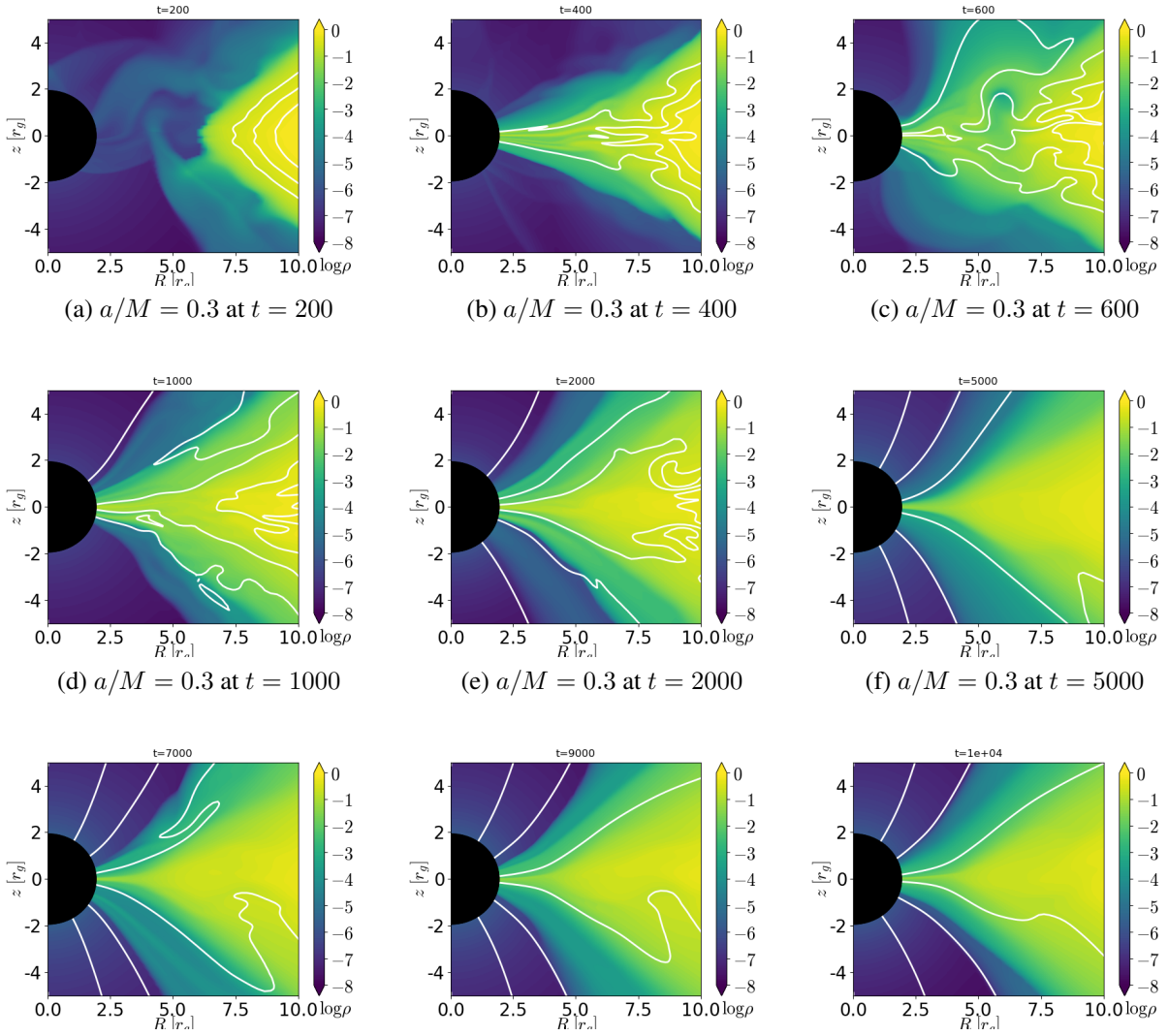

(a) $a/M = 0.3$ at $t = 200$ (b) $a/M = 0.3$ at $t = 400$ (c) $a/M = 0.3$ at $t = 600$

(d) $a/M = 0.3$ at $t = 1000$ (e) $a/M = 0.3$ at $t = 2000$ (f) $a/M = 0.3$ at $t = 5000$

(g) $a/M = 0.3$ at $t = 7000$ (h) $a/M = 0.3$ at $t = 9000$ (i) $a/M = 0.3$ at $t = 10000$

Figure A.3: Evolution of a torus with $a/M = 0.3$ at certain time steps

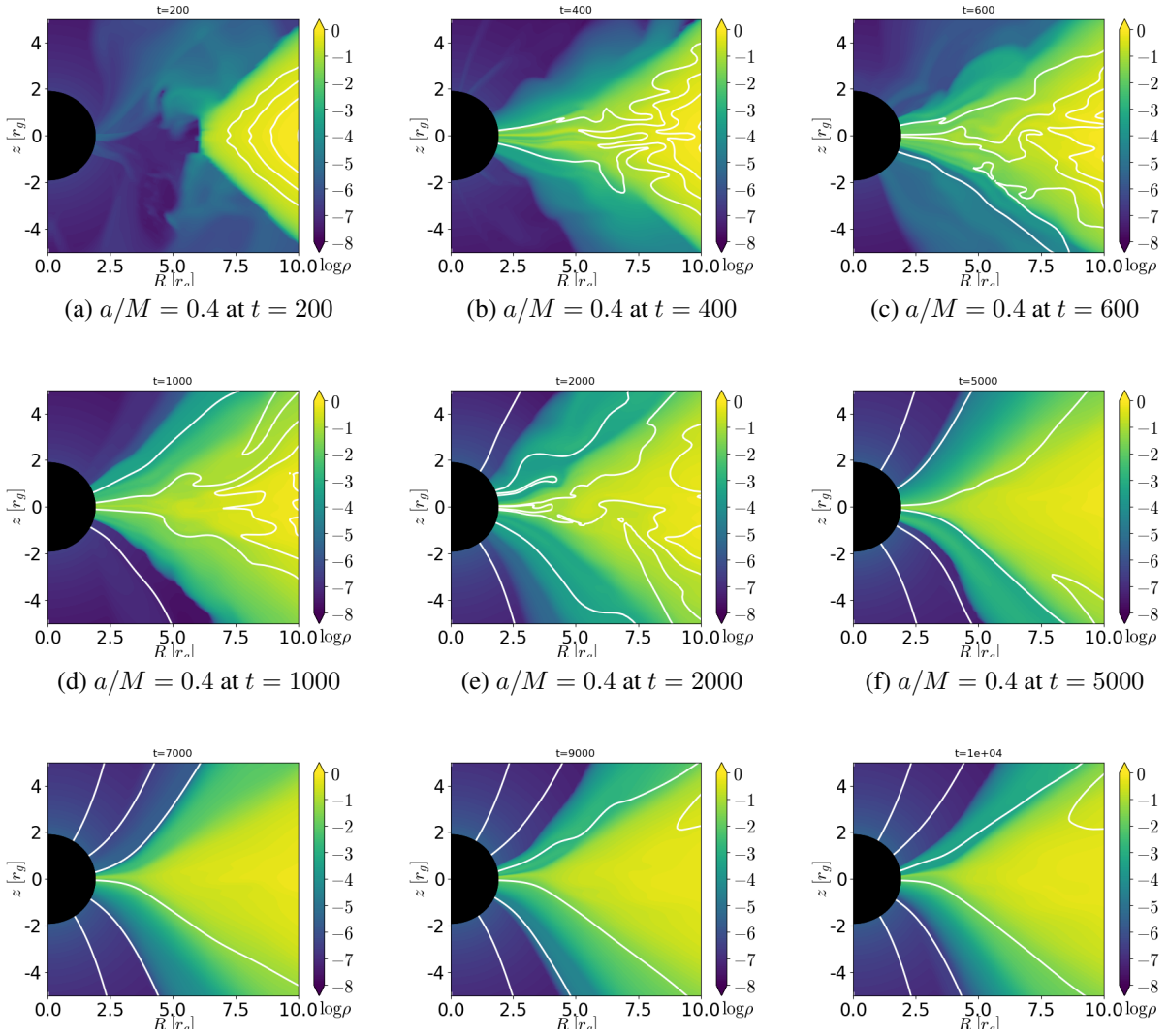

(a) $a/M = 0.4$ at $t = 200$ (b) $a/M = 0.4$ at $t = 400$ (c) $a/M = 0.4$ at $t = 600$

(d) $a/M = 0.4$ at $t = 1000$ (e) $a/M = 0.4$ at $t = 2000$ (f) $a/M = 0.4$ at $t = 5000$

(g) $a/M = 0.4$ at $t = 7000$ (h) $a/M = 0.4$ at $t = 9000$ (i) $a/M = 0.4$ at $t = 10000$

Figure A.4: Evolution of a torus with $a/M = 0.4$ at certain time steps

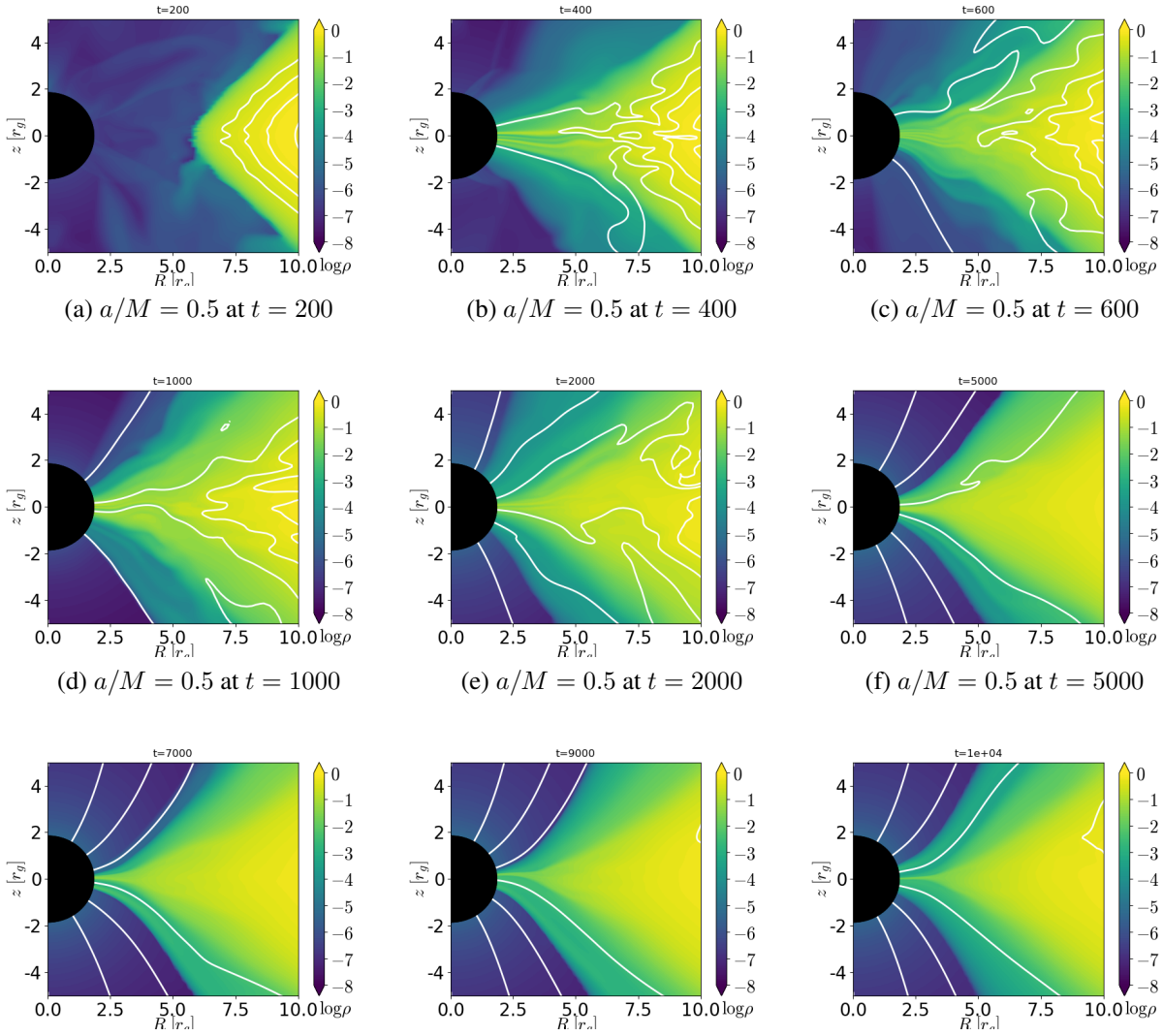

(a) $a/M = 0.5$ at $t = 200$ (b) $a/M = 0.5$ at $t = 400$ (c) $a/M = 0.5$ at $t = 600$

(d) $a/M = 0.5$ at $t = 1000$ (e) $a/M = 0.5$ at $t = 2000$ (f) $a/M = 0.5$ at $t = 5000$

(g) $a/M = 0.5$ at $t = 7000$ (h) $a/M = 0.5$ at $t = 9000$ (i) $a/M = 0.5$ at $t = 10000$

Figure A.5: Evolution of a torus with $a/M = 0.5$ at certain time steps

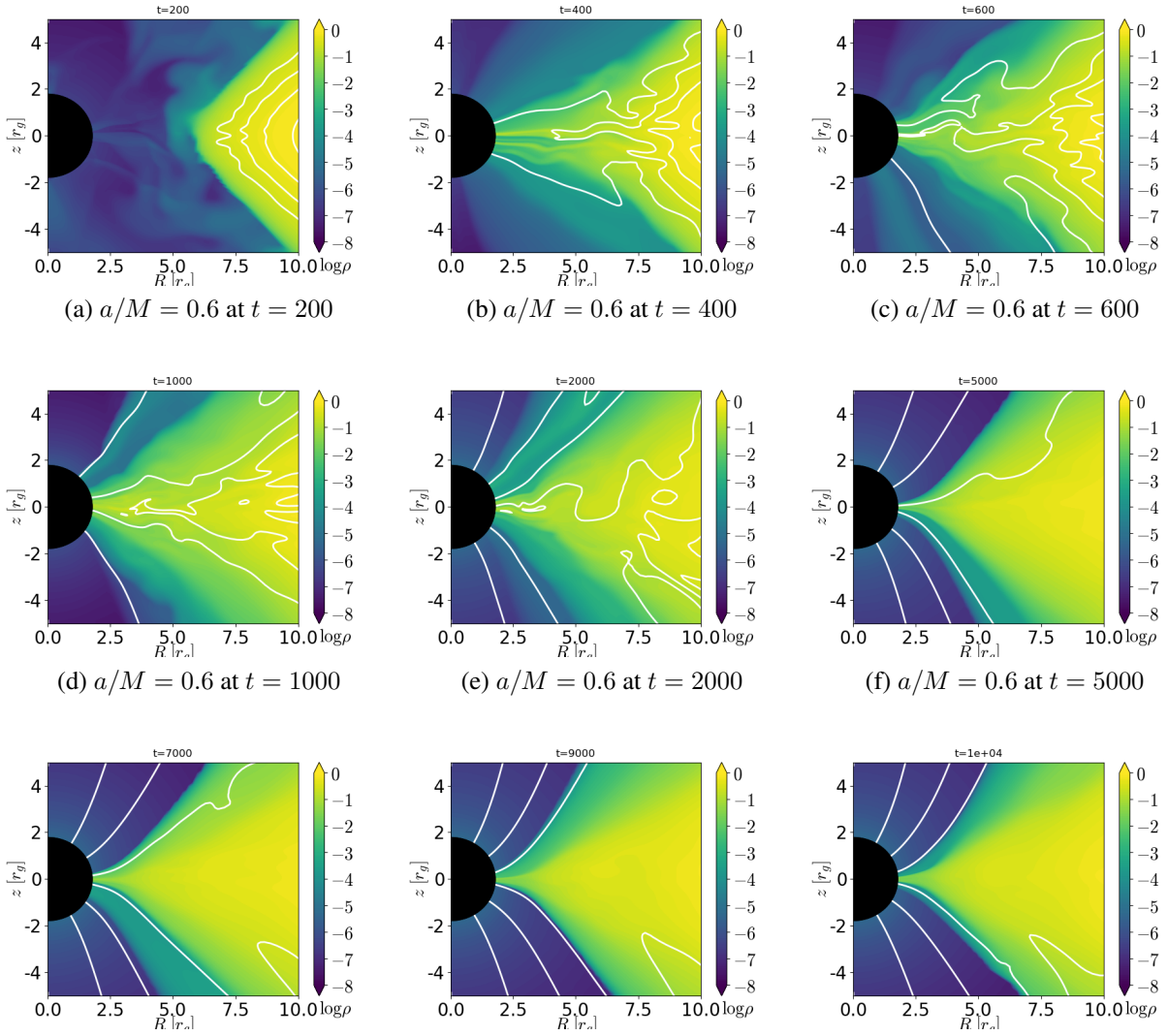

(a) $a/M = 0.6$ at $t = 200$ (b) $a/M = 0.6$ at $t = 400$ (c) $a/M = 0.6$ at $t = 600$

(d) $a/M = 0.6$ at $t = 1000$ (e) $a/M = 0.6$ at $t = 2000$ (f) $a/M = 0.6$ at $t = 5000$

(g) $a/M = 0.6$ at $t = 7000$ (h) $a/M = 0.6$ at $t = 9000$ (i) $a/M = 0.6$ at $t = 10000$

Figure A.6: Evolution of a torus with $a/M = 0.6$ at certain time steps

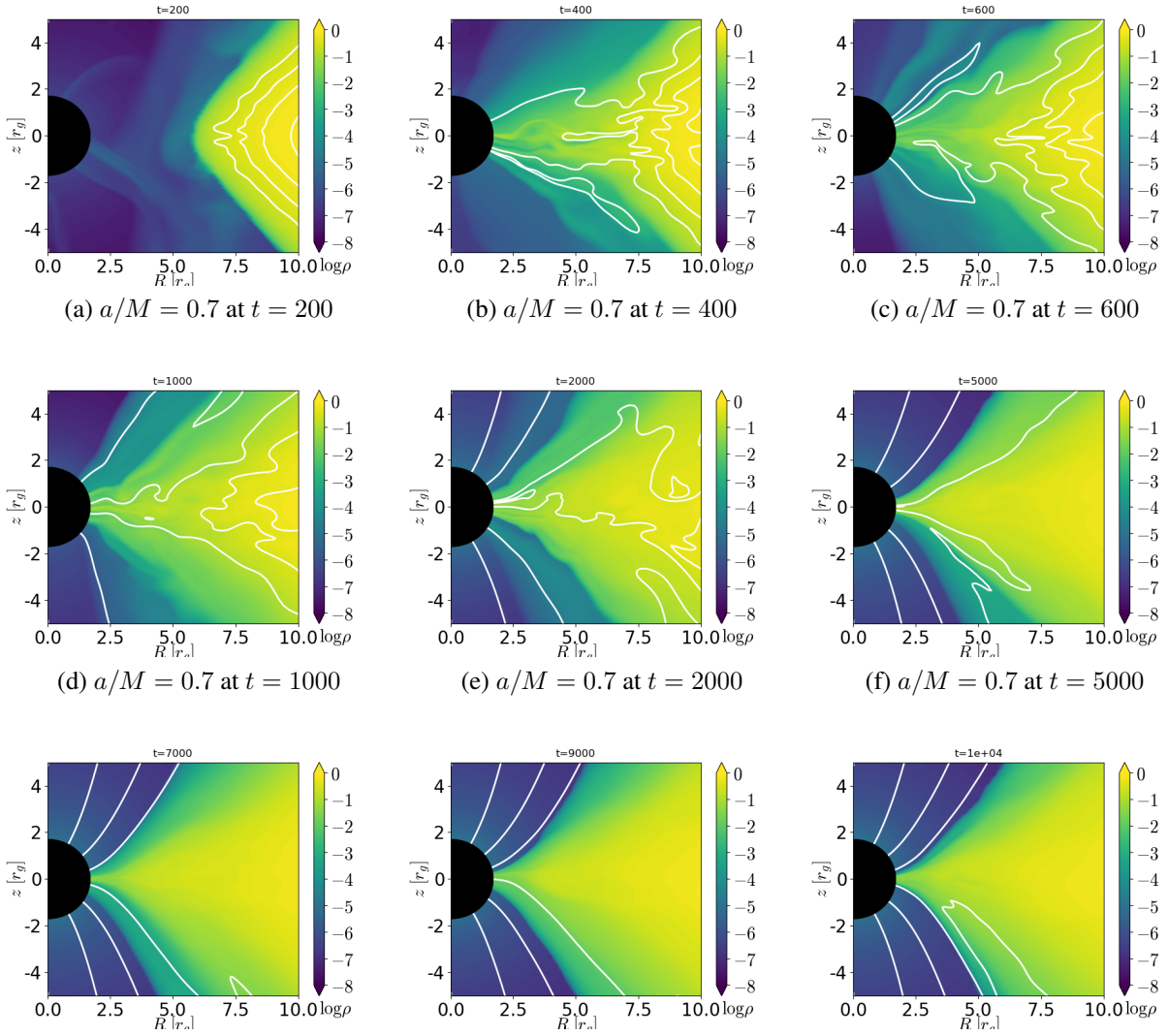

(a) $a/M = 0.7$ at $t = 200$ (b) $a/M = 0.7$ at $t = 400$ (c) $a/M = 0.7$ at $t = 600$

(d) $a/M = 0.7$ at $t = 1000$ (e) $a/M = 0.7$ at $t = 2000$ (f) $a/M = 0.7$ at $t = 5000$

(g) $a/M = 0.7$ at $t = 7000$ (h) $a/M = 0.7$ at $t = 9000$ (i) $a/M = 0.7$ at $t = 10000$

Figure A.7: Evolution of a torus with $a/M = 0.7$ at certain time steps

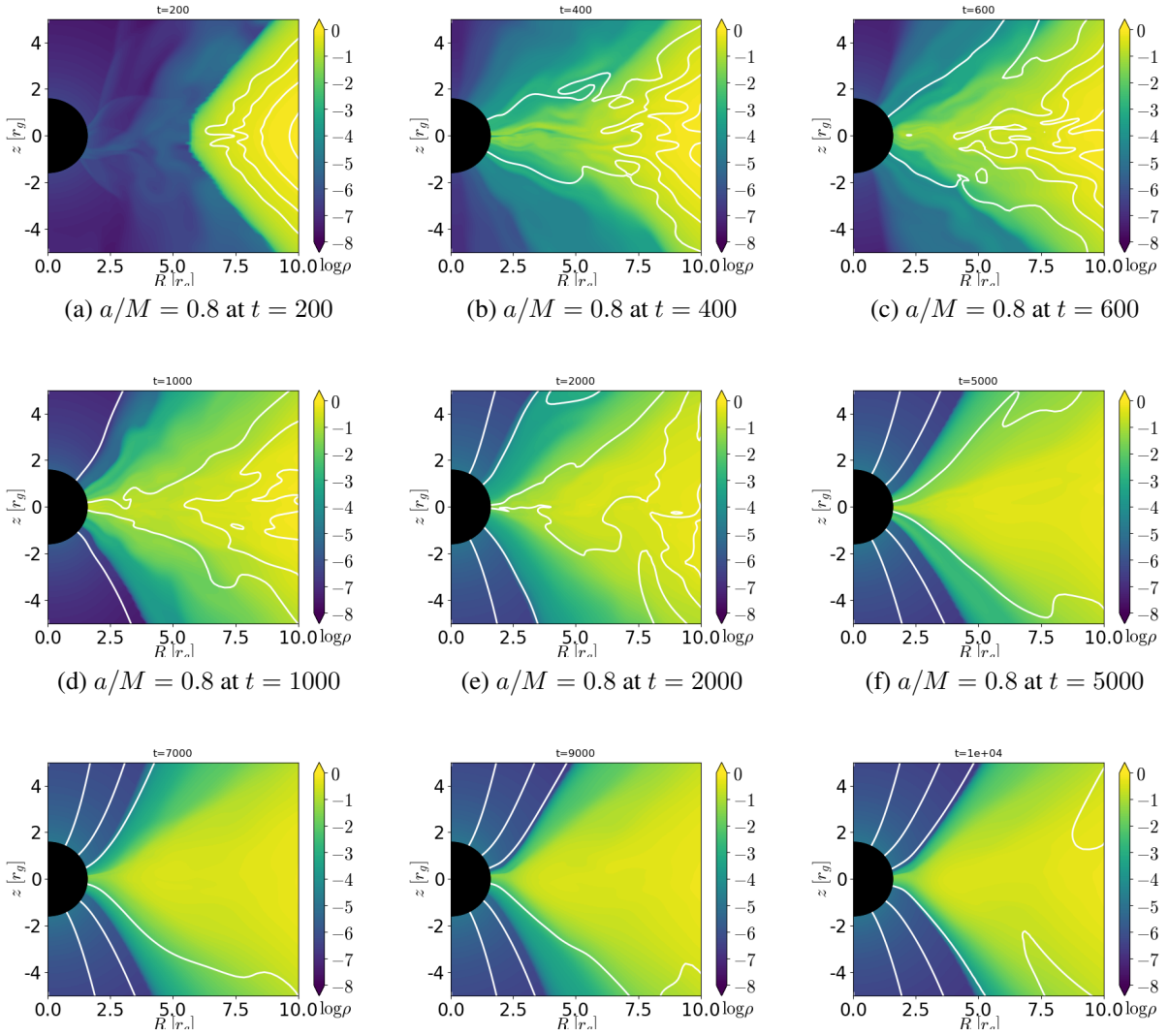

(a) $a/M = 0.8$ at $t = 200$ (b) $a/M = 0.8$ at $t = 400$ (c) $a/M = 0.8$ at $t = 600$

(d) $a/M = 0.8$ at $t = 1000$ (e) $a/M = 0.8$ at $t = 2000$ (f) $a/M = 0.8$ at $t = 5000$

(g) $a/M = 0.8$ at $t = 7000$ (h) $a/M = 0.8$ at $t = 9000$ (i) $a/M = 0.8$ at $t = 10000$

Figure A.8: Evolution of a torus with $a/M = 0.8$ at certain time steps

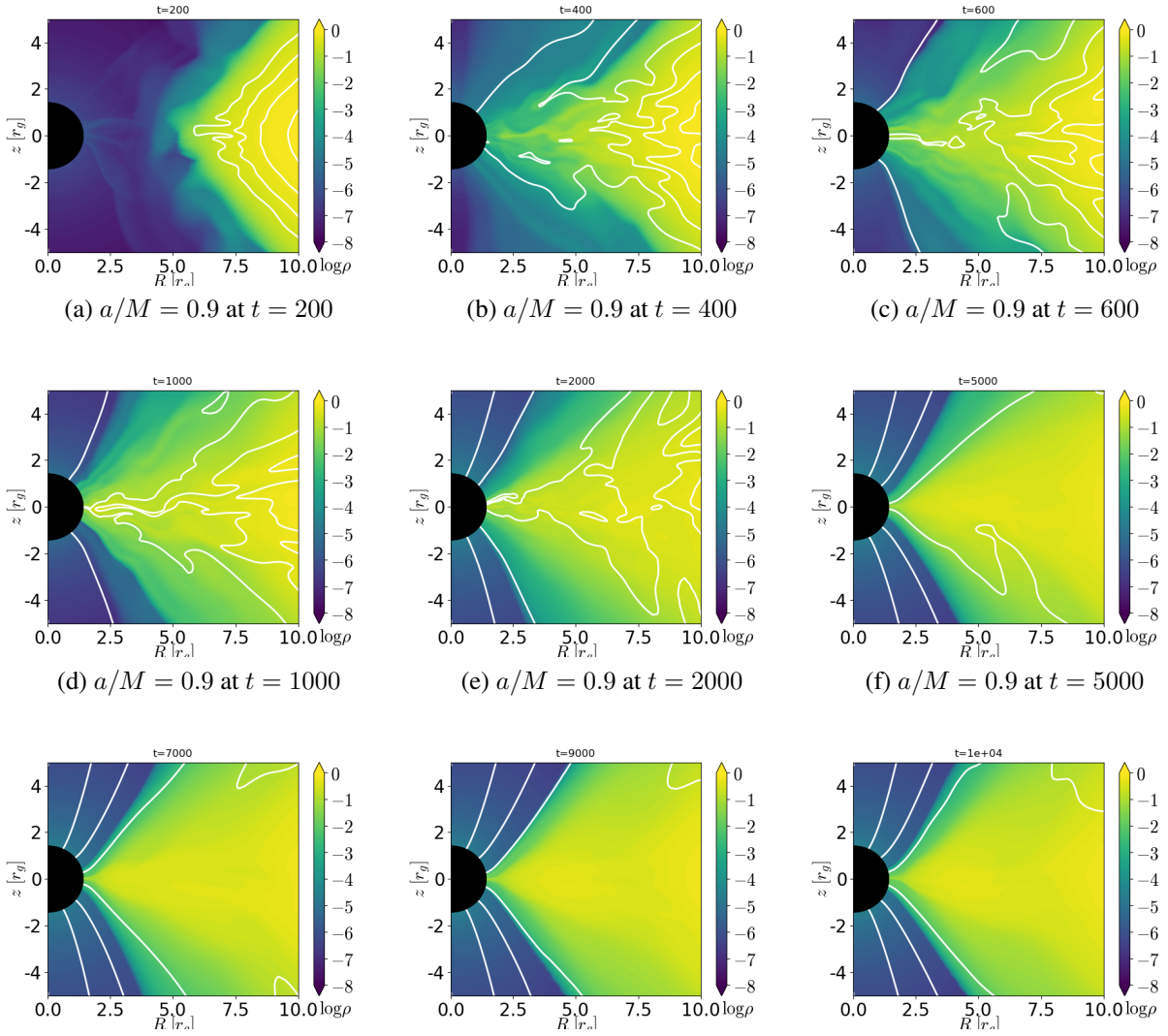

(a) $a/M = 0.9$ at $t = 200$ (b) $a/M = 0.9$ at $t = 400$ (c) $a/M = 0.9$ at $t = 600$

(d) $a/M = 0.9$ at $t = 1000$ (e) $a/M = 0.9$ at $t = 2000$ (f) $a/M = 0.9$ at $t = 5000$

(g) $a/M = 0.9$ at $t = 7000$ (h) $a/M = 0.9$ at $t = 9000$ (i) $a/M = 0.9$ at $t = 10000$

Figure A.9: Evolution of a torus with $a/M = 0.9$ at certain time steps

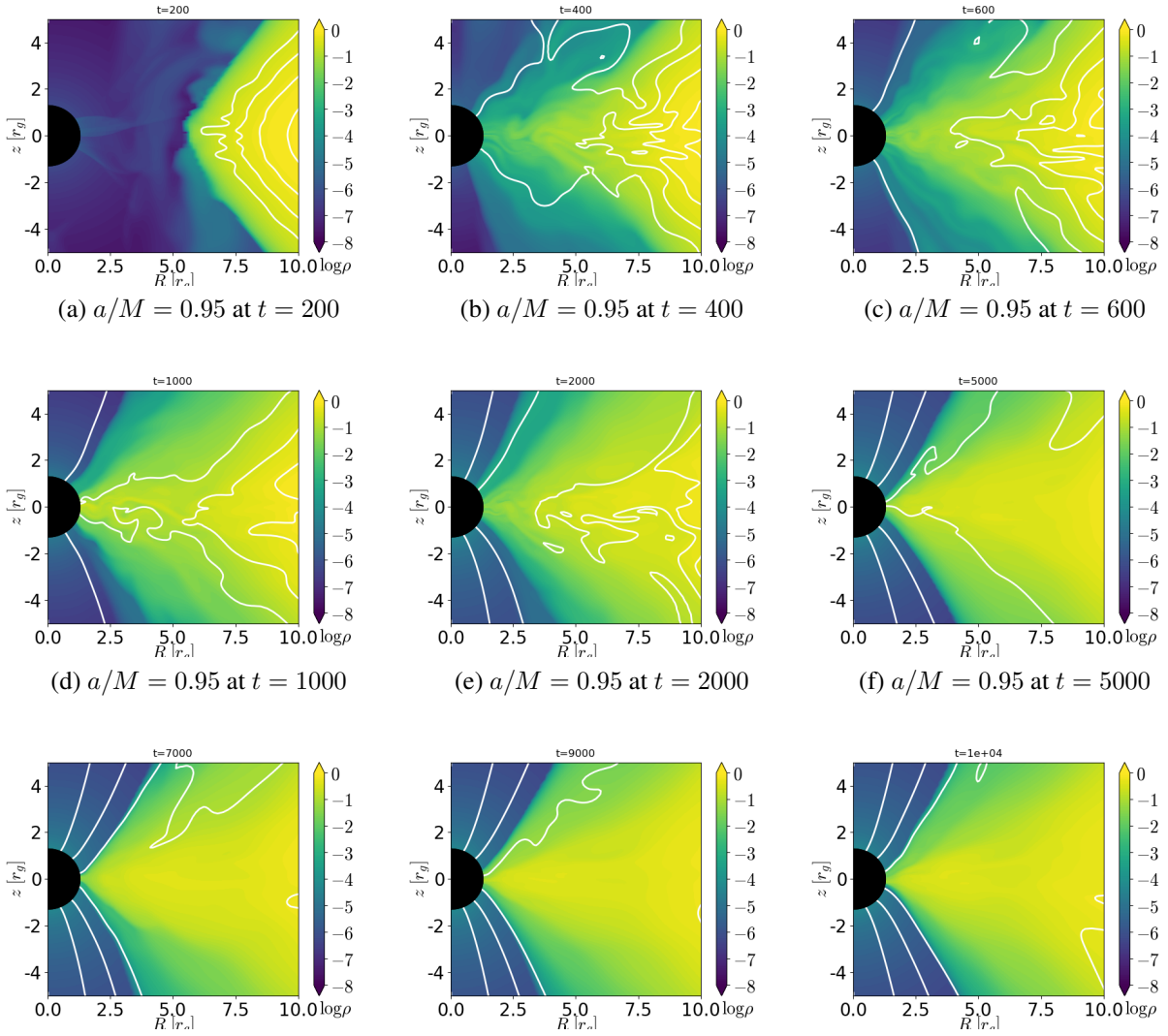

(a) $a/M = 0.95$ at $t = 200$ (b) $a/M = 0.95$ at $t = 400$ (c) $a/M = 0.95$ at $t = 600$

(d) $a/M = 0.95$ at $t = 1000$ (e) $a/M = 0.95$ at $t = 2000$ (f) $a/M = 0.95$ at $t = 5000$

(g) $a/M = 0.95$ at $t = 7000$ (h) $a/M = 0.95$ at $t = 9000$ (i) $a/M = 0.95$ at $t = 10000$

Figure A.10: Evolution of a torus with $a/M = 0.95$ at certain time steps

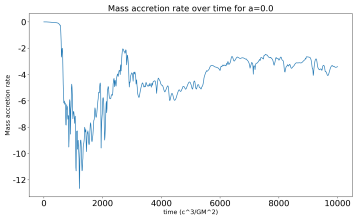

(a) $a/M = 0.0$

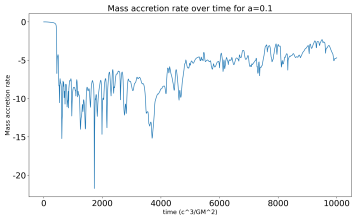

(b) $a/M = 0.91$

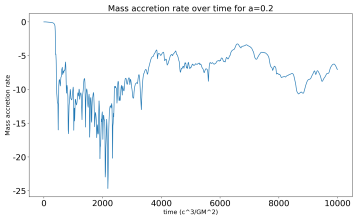

(c) $a/M = 0.2$

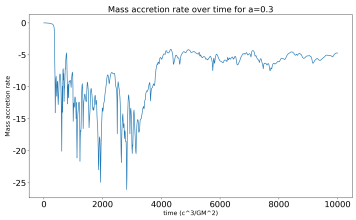

(d) $a/M = 0.3$

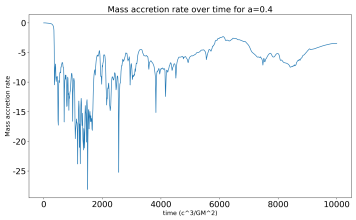

(e) $a/M = 0.4$

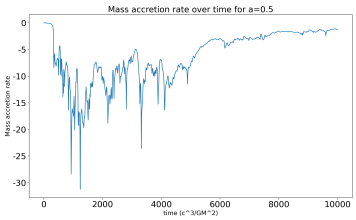

(f) $a/M = 0.5$

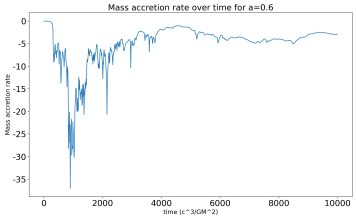

(g) $a/M = 0.6$

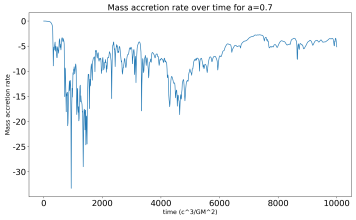

(h) $a/M = 0.7$

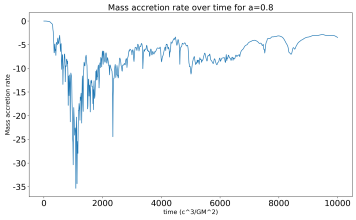

(i) $a/M = 0.8$

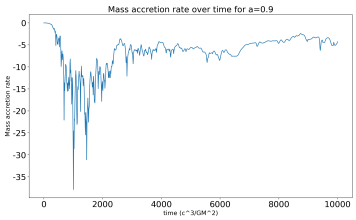

(j) $a/M = 0.9$

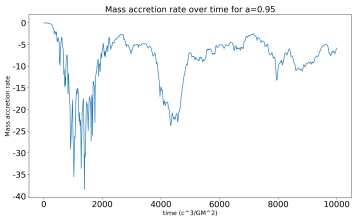

(k) $a/M = 0.95$

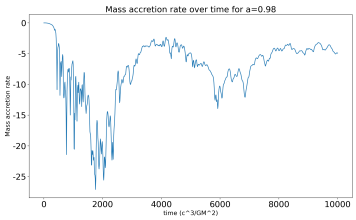

(l) $a/M = 0.98$

Figure A.11: Accretion rate over time for different spin parameters

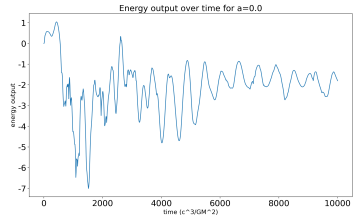

(a) $a/M = 0.0$

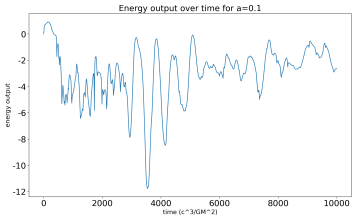

(b) $a/M = 0.1$

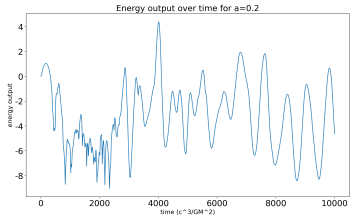

(c) $a/M = 0.2$

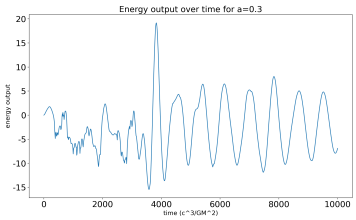

(d) $a/M = 0.3$

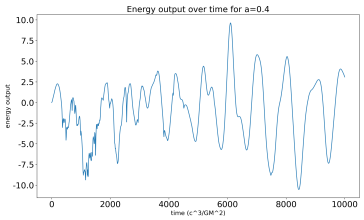

(e) $a/M = 0.4$

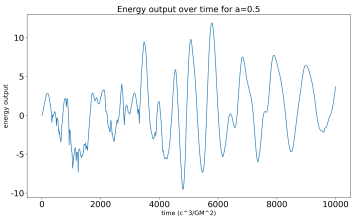

(f) $a/M = 0.5$

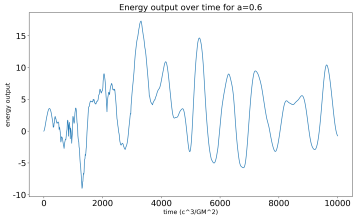

(g) $a/M = 0.6$

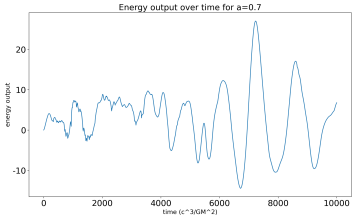

(h) $a/M = 0.7$

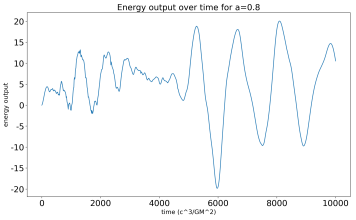

(i) $a/M = 0.8$

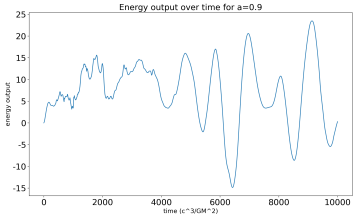

(j) $a/M = 0.9$

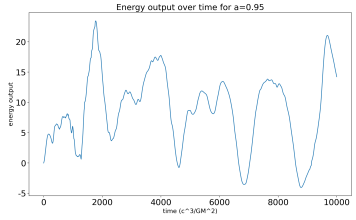

(k) $a/M = 0.95$

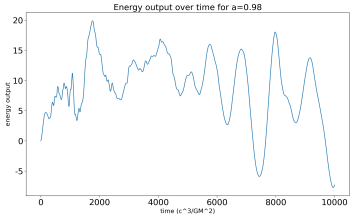

(l) $a/M = 0.98$

Figure A.12: Energy output over time for different spin parameters

References

[1] Jongho Park, Kazuhiro Hada, Motoki Kino, Masanori Nakamura, Hyunwook Ro, and Sascha Trippe. Faraday rotation in the jet of m87 inside the bondi radius: indication of winds from hot accretion flows confining the relativistic jet. *The Astrophysical Journal*, 871(2):257, 2019.

[2] David L. Meier, Shinji Koide, and Yutaka Uchida. Magnetohydrodynamic production of relativistic jets. *Science*, 291(5501):84–92, 2001.

[3] A. Rosa, Phil Uttley, Lijun Gou, Yuan Liu, Cosimo Bambi, Didier Barret, Tomaso Belloni, Emanuele Berti, Stefano Bianchi, Ilaria Caiazzo, Piergiorgio Casella, Marco Feroci, Valeria Ferrari, Leonardo Gualtieri, Jeremy Heyl, Adam Ingram, Vladimir Karas, Fangjun Lu, Bin Luo, and Xinlin Zhou. Accretion in strong field gravity with extp. *Science China Physics, Mechanics & Astronomy*, 62, 12 2018.

[4] Tejinder P Singh. Gravitational collapse, black holes and naked singularities. *Journal of Astrophysics and Astronomy*, 20(3-4):221–232, 1999.

[5] John Kormendy and Luis C. Ho. Coevolution (or not) of supermassive black holes and host galaxies. *Annual Review of Astronomy and Astrophysics*, 51(1):511–653, Aug 2013.

[6] Ramesh Narayan and Eliot Quataert. Black hole accretion. *Science*, 307(5706):77–80, 2005.

[7] M Samadi, S Zanganeh, and S Abbassi. Bondi accretion in the finite luminous region of elliptical galaxies. *Monthly Notices of the Royal Astronomical Society*, 489(3):3870–3878, 09 2019.

[8] Roger Blandford, David Meier, and Anthony Readhead. Relativistic jets from active galactic nuclei. *Annual Review of Astronomy and Astrophysics*, 57(1):467–509, 2019.

[9] RD Blandford and DG Payne. Hydromagnetic flows from accretion discs and the production of radio jets. *Monthly Notices of the Royal Astronomical Society*, 199(4):883–903, 1982.

[10] Roger D Blandford and Roman L Znajek. Electromagnetic extraction of energy from kerr black holes. *Monthly Notices of the Royal Astronomical Society*, 179(3):433–456, 1977.

[11] S. W. Allen, R. J. H. Dunn, A. C. Fabian, G. B. Taylor, and C. S. Reynolds. The relation between accretion rate and jet power in X-ray luminous elliptical galaxies. *Monthly Notices of the Royal Astronomical Society*, 372(1):21–30, 09 2006.

[12] HC Spruit. Essential magnetohydrodynamics for astrophysics. *arXiv preprint arXiv:1301.5572*, 2013.

[13] JOHANNES KEPLER. Introduction to magnetohydrodynamics.

[14] Juan Hernandez and Pavel Kovtun. Relativistic magnetohydrodynamics. *Journal of High Energy Physics*, 2017(5):1, 2017.

[15] Matthew Liska, Koushik Chatterjee, Alexander Tchekhovskoy, Doosoo Yoon, David van Eijnatten, Casper Hesp, Sera Markoff, Adam Ingram, and Michiel van der Klis. H-amr: A new

gpu-accelerated grmhd code for exascale computing with 3d adaptive mesh refinement and local adaptive time-stepping. *arXiv preprint arXiv:1912.10192*, 2019.

[16] Steven A Balbus and John F Hawley. A powerful local shear instability in weakly magnetized disks: I. linear analysis. In *Bulletin of the American Astronomical Society*, volume 22, page 1209, 1990.

[17] Jason Dexter, Eric Agol, P Chris Fragile, and Jonathan C McKinney. Radiative models of sagittarius a* and m87 from relativistic mhd simulations. In *Journal of Physics: Conference Series*, volume 372, page 012023. IOP Publishing, 2012.

[18] Charles F Gammie, Jonathan C McKinney, and Gábor Tóth. Harm: a numerical scheme for general relativistic magnetohydrodynamics. *The Astrophysical Journal*, 589(1):444, 2003.

[19] Alexander Tchekhovskoy. Harmpi: 3d massively parallel general relativictic mhd code. *Astrophysics Source Code Library*, pages ascl–1912, 2019.

[20] Oliver Porth, Koushik Chatterjee, Ramesh Narayan, Charles F Gammie, Yosuke Mizuno, Peter Anninos, John G Baker, Matteo Bugli, Chi-kwan Chan, Jordy Davelaar, et al. The event horizon general relativistic magnetohydrodynamic code comparison project. *The Astrophysical Journal Supplement Series*, 243(2):26, 2019.

[21] Jonathan C McKinney, Alexander Tchekhovskoy, and Roger D Blandford. General relativistic magnetohydrodynamic simulations of magnetically choked accretion flows around black holes. *Monthly Notices of the Royal Astronomical Society*, 423(4):3083–3117, 2012.

[22] Stuart L Shapiro and Saul A Teukolsky. *Black holes, white dwarfs, and neutron stars: The physics of compact objects*. John Wiley & Sons, 2008.

[23] PM Blakely and Nikolaos Nikiforakis. Relativistic bondi-hoyle-lyttleton accretion: A parametric study. *Astronomy & Astrophysics*, 583:A90, 2015.

[24] August J Miller and Thomas W Baumgarte. Bondi accretion in trumpet geometries. *Classical and Quantum Gravity*, 34(3):035007, 2017.

[25] Sébastien Peirani and José Antonio de Freitas Pacheco. Dark matter accretion into supermassive black holes. *Physical Review D*, 77(6):064023, 2008.

[26] Volker Springel, Tiziana Di Matteo, and Lars Hernquist. Modelling feedback from stars and black holes in galaxy mergers. *Monthly Notices of the Royal Astronomical Society*, 361(3):776–794, 2005.

[27] Andrew J. Benson and Arif Babul. Maximum spin of black holes driving jets. *Monthly Notices of the Royal Astronomical Society*, 397(3):1302–1313, 07 2009.

[28] Charles F. Gammie, Stuart L. Shapiro, and Jonathan C. McKinney. Black hole spin evolution. *The Astrophysical Journal*, 602(1):312–319, feb 2004.

[29] Leon Heller. On the penrose process for rotating black holes, 2009.

[30] Christopher S. Reynolds. Observing black holes spin. *Nature Astronomy*, 3(1):41–47, Jan 2019.

[31] GV Kraniotis. Frame dragging and bending of light in kerr and kerr–(anti) de sitter spacetimes. *Classical and Quantum Gravity*, 22(21):4391, 2005.

[32] David Garofalo. Retrograde versus prograde models of accreting black holes. *Advances in Astronomy*, 2013:213105, Apr 2013.

[33] Parth Bambhaniya, Divyesh N Solanki, Dipanjan Dey, Ashok B Joshi, Pankaj S Joshi, and Vishwa Patel. Precession of timelike bound orbits in kerr spacetime. *arXiv preprint arXiv:2007.12086*, 2020.

[34] JL Blum, JM Miller, AC Fabian, MC Miller, J Homan, M Van Der Klis, EM Cackett, and RC Reis. Measuring the spin of grs 1915+ 105 with relativistic disk reflection. *The Astrophysical Journal*, 706(1):60, 2009.

[35] Xueshan Zhao, Lijun Gou, Yanting Dong, Xueying Zheng, James F Steiner, James CA Miller-Jones, Arash Bahramian, Jerome A Orosz, and Ye Feng. Re-estimating the spin parameter of the black hole in cygnus x-1. *The Astrophysical Journal*, 908(2):117, 2021.

[36] Robert F Penna, Akshay Kulkarni, and Ramesh Narayan. A new equilibrium torus solution and grmhd initial conditions. *Astronomy & Astrophysics*, 559:A116, 2013.

[37] Leslie G Fishbone and Vincent Moncrief. Relativistic fluid disks in orbit around kerr black holes. *The Astrophysical Journal*, 207:962–976, 1976.

[38] Steven W Allen, RJH Dunn, AC Fabian, GB Taylor, and CS Reynolds. The relation between accretion rate and jet power in x-ray luminous elliptical galaxies. *Monthly Notices of the Royal Astronomical Society*, 372(1):21–30, 2006.